Numerical modeling of friction stir welding processes

M. Chiumenti *, M. Cervera, C. Agelet de Saracibar, N. Dialami

International Center for Numerical Methods in Engineering (CIMNE), Universidad Politécnica de Cataluña (UPC), Edificio C1, Campus Norte, Gran Capitán s/n, 08034 Barcelona, Spain

ARTICLE INFO

ABSTRACT

This work describes the formulation adopted for the numerical simulation of the friction stir welding (FSW) process. FSW is a solid-state joining process (the metal is not melted during the process) devised for applications where the original metallurgical characteristics must be retained. This process is primarily used on aluminum alloys, and most often on large pieces which cannot be easily heat treated to recover temper characteristics.

Heat is either induced by the friction between the tool shoulder and the work pieces or generated by the mechanical mixing (stirring and forging) process without reaching the melting point (solid-state process).

To simulate this kind of welding process, a fully coupled thermo-mechanical solution is adopted. A sliding mesh, rotating together with the pin (ALE formulation), is used to avoid the extremely large distortions of the mesh around the tool in the so called stirring zone while the rest of the mesh of the sheet is fixed (Eulerian formulation).

The orthogonal subgrid scale (OSS) technique is used to stabilize the mixed velocity–pressure formulation adopted to solve the Stokes problem. This stabilized formulation can deal with the incompressible behavior of the material allowing for equal linear interpolation for both the velocity and the pressure fields.

The material behavior is characterized either by Norton–Hoff or Sheppard–Wright rigid thermo-visco-plastic constitutive models.

Both the frictional heating due to the contact interaction between the surface of the tool and the sheet, and the heat induced by the visco-plastic dissipation of the stirring material have been taken into account. Heat convection and heat radiation models are used to dissipate the heat through the boundaries.

Both the streamline-upwind/Petrov–Galerkin (SUPG) formulation and the OSS stabilization technique have been implemented to stabilize the convective term in the balance of energy equation.

The numerical simulations presented are intended to show the accuracy of the proposed methodology and its capability to study real FSW processes where a non-circular pin is often used.

1. Introduction

Friction stir welding (FSW) is a solid-state joining process meaning that the metal is not melted during the welding process. In FSW, a shouldered pin is rotated at constant speed and plunged into the joint line between the two metal sheets butted together (see Fig. 1(a) in [51]). Once the tool has been completely inserted, it is moved at constant advancing velocity along the welding line while rotating. During the process operations, a clamping system must keep the work-pieces rigidly fixed onto a backing bar to prevent the abutting joint faces from being forced apart. Due to the rotation and the advancing motion of the pin, the material close

to the tool, in the so called stir-zone, is softened by the heat generated by the plastic dissipation (stirring effect) and the heat induced by the contact friction between the probe shoulders and the sheet. As a consequence, the material is stretched and forged around the rotating probe flowing from the advancing side to the retreating side of the weld, where it can rapidly cool down and consolidate, to create a high quality solid-state weld.

The FSW process was patented at The Welding Institute (UK) in December 1991 [65] and it has proven to be a very successful joining technology for aluminum alloys, nickel alloys and, more recently, for steels [66,29]. The solid-state nature of FSW has several advantages over fusion welding methods since any problems associated with cooling from the liquid phase are avoided. Porosity defects, solidification cracking and liquation cracking do not occur during FSW. Nevertheless, as in the traditional fusion welds, a softened heat affected zone and a tensile residual stress parallel to the

---

* Corresponding author.
E-mail address: michele@cimne.upc.edu (M. Chiumenti).
URL: http://www.cimne.com (M. Chiumenti).

weld do appear. Furthermore, FSW process can suffer for a different class of defects; for instance, due to insufficient welding temperature (low rotational speeds or high advancing speeds) or caused when the weld material, in the stir-zone, is unable to accommodate the extensive deformation during the stirring action. The material flow is very sensitive to the different welding operation parameters (rotation speed, advancing speed, shoulder pressure, pin shape, sheet thickness, among others), which must be carefully calibrated according to the welding operation and the selected material. The strong coupling between the temperature field and the mechanical behavior is the key-point in FSW and its highly non-linear relationship makes the process setup complex. The operative range for most of the welding process parameters is rather narrow, requiring a tedious characterization and sensitivity analysis. This is why, despite the apparent simplicity of this novel welding procedure, computational modeling is considered a very helpful tool to understand the leading mechanisms that govern the material behavior.

To date, most of the research interest devoted to the topic was focused on the heat transfer and thermal analysis in FSW. In [42] the authors proposed a simple heat transfer model to predict the temperature distribution in the work-piece. A moving heat source model for a finite element analysis was developed in [18,19], and the transient evolution of the temperature field, the induced residual stresses and distortions induced by the FSW process were simulated. Three-dimensional heat flow models for the prediction of the temperature field were developed in [25,40]. The effect of the shoulder of the pin on the heat generation during the FSW operation was investigated in [50,59]. Coupled thermo-mechanical modeling of the FSW process was analyzed in [68,49,31,30]. An interesting comparison between the heat energy generated by the FSW using numerical methods and experimental data was presented in [37,20]. From the experimental point of view, different measurements of temperature field of the work-piece can be found in [64], while measured residual stresses in FSW for 2024-T3 and 6013-T6 aluminum are presented in [38]. Experimental evidence of the material flow around the tool by using copper sheets placed transversally and longitudinally to the weld line is shown in [32,43]. In these works the flow pattern is characterized by using metallography, 2D X-rays analysis and X-rays tomography, showing that copper sheets embedded into the aluminum work-pieces could be successfully used as marker material. Finally, a demonstration of the tremendous potential and successful applications of the FSW process for aluminum airframe structures was presented in [63].

The effort devoted to understand the leading mechanisms within the FSW process making use of the numerical simulation often presents some limitations in terms of complexity of the pin geometry, non-linearity of the material behavior or ad hoc boundary conditions. In this work, a fully coupled thermo-mechanical framework for the numerical simulation of the FSW process is presented. The strategy adopted to deal with a generic pin shape (not necessarily cylindrical) together with an accurate definition of the boundary conditions is presented in Section 2. The local (strong) form of the momentum, mass and energy balance equations, which govern the thermo-mechanical problem, is presented in Section 3. In this Section, two alternative rigid-visco-plastic models are introduced to deal with the extremely large deformation rates occurring in a FSW process. Both models have been coupled with the temperature field to consider the thermal softening behavior of the material during the stirring process. Section 4 presents the staggered solution adopted to solve the coupled problem within the framework of the classical fractional step method. The resulting time integration scheme is based on the isothermal operator split of the governing equations. The weak (integral) form of the thermo-mechanical governing equations is

presented in Section 5. On one hand, the mechanical problem is solved by the balance of momentum equation together with the mass continuity equation to force the incompressibility constraint. This mechanical constraint is necessary when the deformation experimented by the material is mainly (or exclusively) deviatoric, that is, preserving the original volume. To this end, an ad hoc stabilization technique based on the orthogonal sub-grid scale (OSS) methods is introduced to overcome the Inf-Sup condition (on the choice of the interpolation spaces) allowing the use of linear–linear interpolations for both velocities and pressure fields. On the other hand, the weak form of the thermal problem is also manipulated to introduce the necessary stabilization for the convective term. Also in this case, the stabilization approach is based on the OSS technique. In Section 6, the frictional contact between the pin and the stir zone as well as the interaction between the work-piece and the stir-zone is detailed. Both the classical Coulomb's law and the Norton's friction law are presented together with the corresponding heat flux generated by the friction dissipation. Finally, two numerical benchmarks are presented in Section 7 to assess the present formulation and to show its performance.

2. Numerical strategy to simulate the FSW process

In this section, the strategy adopted for the numerical simulation of the FSW process is presented. Firstly, it is important to distinguish between two different kinds of analyses carried out at *local* or *global* level, respectively.

On one hand, we refer to local level analysis when the focus of the simulation is the stirring zone. This class of simulation is intended to compute the heat power generated either by the visco-plastic dissipation induced by the stirring process or by the friction at the contact interface between the probe shoulder and the metal sheet. At this level, different phenomena directly related to the FSW technology can be studied: the relationship between rotation and advancing speed, the contact mechanisms in terms of applied normal pressure and friction coefficient, the pin shape, the material flow within the heat affected zone (HAZ), the size of the HAZ and the corresponding consequences on the microstructure evolution, etc.

On the other hand, a simulation carried out at global level studies the entire structure to be welded. A moving heat power source is applied to a control volume representing the actual size of the heat affected zone at each time-step of the analysis. The effects induced by the FSW process on the structural behavior are the target of this kind of study. These effects can show in terms of distortions, residual stresses or weaknesses along the welding line, among others.

In this work, a novel numerical strategy to model the FSW process at local level is presented. Fig. 1b) shows three different zones used to distinguish among pin (green), stir-zone (blue[1]) and the rest of the work-piece (gray). Taking into account that, during the welding process, the pin is rotating at a very high speed (e.g. 50–1500 rpm, depending on the work-piece material), a fully Lagrangian approach (which follows the material particles of the continuum in their motion) is unaffordable. The material in the stirring zone suffers very large deformations at high strain-rates. Consequently, a continuous re-meshing is required to avoid excessive mesh distortions. This would lead to high computational costs, as well as to a general loss of solution accuracy due to the interpolation process necessary to move both nodal and Gaussian variables from mesh to mesh.

---

[1] For interpretation of color in Figs. 1–4, the reader is referred to the web version of this article.

(a) FSW process technology

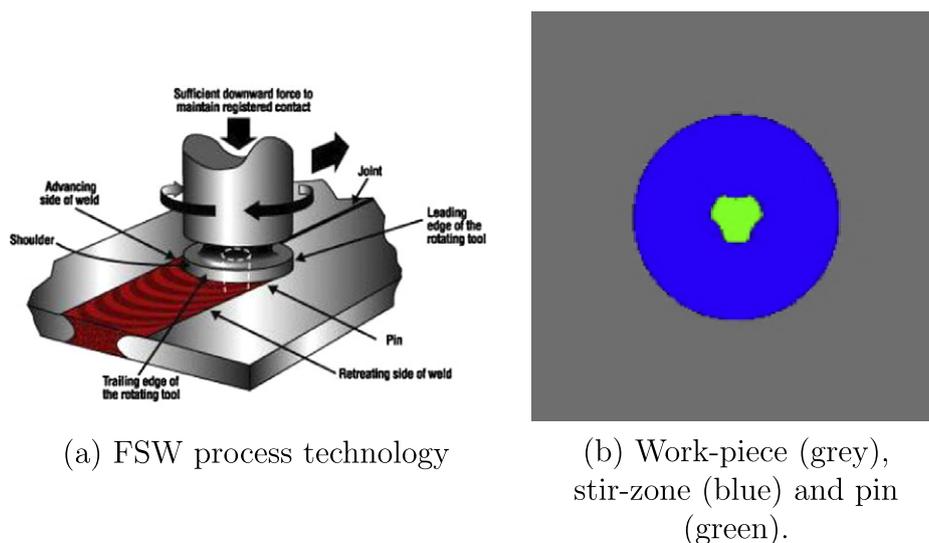(b) Work-piece (grey), stir-zone (blue) and pin (green).

Fig. 1. FSW technology and computational domains.

The alternative is the Eulerian approach (which looks at spatial positions instead of material points). Velocities are used as nodal variables (rather than displacements) and the constitutive laws are typically formulated in terms of strain-rate rather than strain. Hence, instead of a thermo-elasto-visco-plastic model (generally adopted for metals in the Lagrangian formulation), a thermo-rigid-visco-plastic behavior is usually introduced within an Eulerian framework.

A further complexity to be taken into account when modeling a FSW process is the shape of the pin. Within an Eulerian framework, when the pin is not cylindrical, the boundaries of the model are continuously changing according to the current position/rotation of the pin. As a consequence, the integration domain must be re-defined at each time-step of the simulation. In this work, an *Arbitrary-Lagrangian–Eulerian* formulation (ALE) is used (see survey in [36]). The reference system is rigidly rotated following the pin movement (*convective* frame) independently of the material points. Using this procedure, re-meshing is avoided in the stir-zone, and a convective term must be added to the balance equations.

The first papers introducing the Arbitrary–Lagrangian–Eulerian formulation date back to 1964 with the original name of coupled Eulerian–Lagrangian [52] and mixed Eulerian–Lagrangian [39], respectively. They implemented their formulations in a finite difference code. More recently, the ALE formulation has been introduced in the FE community for fluid–structure interaction analysis by Donéa [33–35], Belytschko [10–12] and Hughes [47] among others. The method has been further extended to solid mechanics [55,45,56,58,13]. Finally, within the context of FSW process the ALE formulation has been used by De Vuyst et al. [30,31], Santiago et al. [60,61] among others.

The description of motion and the corresponding simulation strategy adopted for the work-piece (the stir-zone excluded), the stir-zone and the pin is quite different.

To this end, let us distinguish between:

- **x**: the coordinates of a *point* in space (referred to as a *spatial point*), defined by the Cartesian reference system, $R_{\mathbf{x}}$. This reference system does not move (inertial system) and it is referred to as the *Eulerian* system. If a body is moving in $R_{\mathbf{x}}$, then its *absolute* velocity is $\mathbf{v} = \frac{d\mathbf{x}}{dt}$;

- **X**: the location of a *particle* (referred to as a *material point*) of the body. This is the *Lagrangian* viewpoint used to identify the material domain, $R_{\mathbf{X}}$, and to follow its motion. The reference system $R_{\mathbf{X}}$ moves and deforms together with the body;

- **χ**: the *convected points* within the *convective* frame R_χ. In the most general case, this reference system moves with a velocity, $\mathbf{v}_{mesh}$, independently of the body motion: this is also referred to as the *Arbitrary-Lagrangian–Eulerian* (ALE) framework. In R_χ the velocity, $\mathbf{v}_\chi = \frac{d\chi}{dt}$, is *relative* to the convective frame R_χ. Observe that, once introduced the FE discretization, the mesh is defined in R_χ and the mesh nodes are neither material points nor spatial points.

This given, let us introduce the definition of motion and deformation within the three different FSW zones.

2.1. Work-piece

The movement of the pin is split into advancing speed (assigned to the work-piece in the opposite direction) and rotation (assigned to the pin). Therefore, the work-piece can be solved within an *Eulerian* framework where the velocity field, $\mathbf{v}(\mathbf{x}, t)$, is the unknown at any *spatial* position, $\mathbf{x}$. The boundary conditions of the problem are given in term of a (prescribed) advancing velocity at the inflow, $\mathbf{v} = \bar{\mathbf{v}}$.

The integration domain, R_χ (the FE mesh), is defined in the Eulerian reference system, $R_{\mathbf{x}}$, so that the nodes of the grid are spatial points: $\chi = \mathbf{x}$, and the velocity of this mesh, $\mathbf{v}_{mesh} = \mathbf{0}$. A particle, $\mathbf{X}$, of the work-piece moves with respect to the mesh and to know its *current position*, $\mathbf{x}(\mathbf{X}, t)$, at time t, it is necessary to integrate the velocity field as:

$$\mathbf{x}(\mathbf{X}, t) = \mathbf{X} + \int_0^t \mathbf{v}(\mathbf{X}, t) dt, \tag{1}$$

where $\mathbf{X} = \mathbf{x}(t = 0)$ is the *reference* position of the particle at time $t = 0$. This integration is necessary to compare the numerical results with the position of the markers introduced in the experimental setting to follow the material stirring during the FSW process.

The balance equations that govern the thermo-mechanical problem require the evaluation of the material time derivatives of both momentum and energy (spatial) fields, $\rho\mathbf{v}$ and ρe respectively, as well as the (spatial) density, ρ.

For the sake of simplicity, let us denote as $\phi(\boldsymbol{\chi}, t)$ a generic state variable of the problem, defined at a node of the mesh $\boldsymbol{\chi}$ at time t. The material time derivative of ϕ is computed as:

$$\left.\frac{D\phi}{Dt}\right|_{\boldsymbol{\chi}=\mathbf{X}} = \left.\frac{\partial\phi}{\partial t}\right|_{\boldsymbol{\chi}=\mathbf{x}} + \frac{\partial\phi}{\partial\boldsymbol{\chi}} \cdot \frac{\partial\boldsymbol{\chi}}{\partial t} \tag{2}$$

$$= \left.\frac{\partial\phi}{\partial t}\right|_{\boldsymbol{\chi}=\mathbf{x}} + \frac{\partial\phi}{\partial\mathbf{x}} \cdot \frac{\partial\mathbf{x}}{\partial t} \tag{3}$$

$$= \left.\frac{\partial\phi}{\partial t}\right|_{\boldsymbol{\chi}=\mathbf{x}} + \mathbf{v}(\mathbf{x}, t) \cdot \nabla_{\mathbf{x}}(\phi) \tag{4}$$

where $\mathbf{v}(\mathbf{x}, t) := \frac{\partial\mathbf{x}(\mathbf{X}, t)}{\partial t}$ is the (spatial) velocity, while $\left.\frac{\partial(\circ)}{\partial t}\right|_{\boldsymbol{\chi}=\mathbf{x}}$ and $\nabla_{\mathbf{x}}(\circ) = \frac{\partial(\circ)}{\partial\mathbf{x}}$ are the spatial time derivative and the spatial gradient, respectively. The second term in (4) is the so called *convective* term. It accounts for the movement of the particle with respect to a fixed grid defined in the reference system, $R_{\mathbf{x}}$. The gradient, $\nabla_{\boldsymbol{\chi}}(\circ) = \nabla_{\mathbf{x}}(\circ)$, needs to be computed only once according to the mesh coordinates defined for the work-piece.

2.2. Pin

A different strategy is adopted for the numerical simulation of the pin. In this case, it is helpful to follow the body movement with the integration domain: at each time-step of the analysis the mesh moves according to the rotation of the pin. Hence, the pin movement is described in a *Lagrangian* framework. The integration domain, $R_{\boldsymbol{\chi}}$ (the finite element mesh), is kept solidary with the tool and it deforms with it. The material particles $\mathbf{X}$, in $R_{\mathbf{X}}$, are permanently connected to the nodes of the grid: $\boldsymbol{\chi} = \mathbf{X}$.

The body motion, referred to the inertial system, is defined by the current position, $\mathbf{x}(\mathbf{X}, t)$ of a particle $\mathbf{X}$, at time, t, as:

$$\mathbf{x}(\mathbf{X}, t) = \mathbf{X} + \mathbf{u}(\mathbf{X}, t), \tag{5}$$

where $\mathbf{u}(\mathbf{X}, t)$ is the (material) displacement field, which is the variable for the mechanical problem.

The material time derivative of a (material) variable, $\phi(\mathbf{X}, t)$, is:

$$\left.\frac{D\phi}{Dt}\right|_{\boldsymbol{\chi}=\mathbf{X}} = \left.\frac{\partial\phi}{\partial t}\right|_{\boldsymbol{\chi}=\mathbf{X}}. \tag{6}$$

Since in the Lagrangian framework the material points coincide with the grid points all along the whole motion, there are no convective effects and the material derivative reduces to a simple time derivative.

The spatial gradient is computed as:

$$\nabla_{\mathbf{x}}(\circ) = \frac{\partial(\circ)}{\partial\mathbf{x}} = \frac{\partial(\circ)}{\partial\mathbf{X}} \cdot \frac{\partial\mathbf{X}}{\partial\mathbf{x}} = \mathbf{F}^{-T} \cdot \nabla_{\mathbf{X}}(\circ), \tag{7}$$

where $\mathbf{F} = \frac{\partial\mathbf{x}(\mathbf{X}, t)}{\partial\mathbf{X}}$ is the deformation gradient accounting for the deformation of the grid, while $\nabla_{\mathbf{X}}(\circ)$ is the material gradient computed at the original position of the mesh, $\mathbf{X} = \mathbf{x}(\mathbf{X}, t = 0)$.

Finally, from Eq. (5), the *material* velocity is computed from the displacement field as:

$$\mathbf{v}(\mathbf{X}, t) := \frac{d\mathbf{x}(\mathbf{X}, t)}{dt} = \frac{d\mathbf{u}(\mathbf{X}, t)}{dt}. \tag{8}$$

2.3. Stir-zone

The stir-zone is part of the work-piece. It is the so called processing zone or heat affected zone (HAZ), where most of the plastic deformations and heat generation occur. The size of this area strongly depends on the viscosity and thermal diffusivity of the material. In a FSW process, particularly after reaching the steady-state conditions, the process zone is restricted to a very close area around the pin. From the numerical simulation point of view, the radius of influence can be taken as 2–3 times the size of the (shouldered) pin.

A more complex description is necessary to study the stir-zone. To avoid continuous remeshing, the grid used to analyze this process zone is (rigidly) rotated following the pin movement. This means that neither the mesh is fixed (as in the Eulerian formulation used for the work-piece), nor it is deforming with the continuum body (as in the Lagrangian framework used for the pin). The integration domain, $R_{\boldsymbol{\chi}}$, moves to keep its boundary connected to the contour surface of the pin. In this case, neither the nodes of the mesh represent material particles nor the velocity of the mesh is equal to the material velocity. This convective framework corresponds to the so called *Arbitrary-Lagrangian–Eulerian* (ALE) setting.

The material derivative of a generic state variable, $\phi(\boldsymbol{\chi}, t)$, is defined as:

$$\left.\frac{D\phi}{Dt}\right|_{\boldsymbol{\chi}=\mathbf{X}} = \left.\frac{\partial\phi}{\partial t}\right|_{\boldsymbol{\chi}} + \frac{\partial\phi}{\partial\boldsymbol{\chi}} \cdot \frac{\partial\boldsymbol{\chi}}{\partial t} = \left.\frac{\partial\phi}{\partial t}\right|_{\boldsymbol{\chi}} + \mathbf{v}_{\boldsymbol{\chi}} \cdot \nabla_{\boldsymbol{\chi}}(\phi). \tag{9}$$

On one hand, the time derivative, $\left.\frac{\partial\phi}{\partial t}\right|_{\boldsymbol{\chi}}$, is computed at the nodes, $\boldsymbol{\chi}$, of the mesh. On the other hand, both the gradient, $\nabla_{\boldsymbol{\chi}}(\circ) = \frac{\partial(\circ)}{\partial\boldsymbol{\chi}}$, and the velocity, $\mathbf{v}_{\boldsymbol{\chi}} = \frac{\partial\boldsymbol{\chi}(\mathbf{X}, t)}{\partial t}$, are referred to the (non-inertial) reference system, $R_{\boldsymbol{\chi}}$. In this ALE framework the convective gradient is expressed by:

$$\nabla_{\boldsymbol{\chi}}(\circ) = \frac{\partial(\circ)}{\partial\boldsymbol{\chi}} = \frac{\partial(\circ)}{\partial\mathbf{x}} \frac{\partial\mathbf{x}}{\partial\boldsymbol{\chi}} = \mathbf{F}_{\boldsymbol{\chi}}^{T} \cdot \nabla_{\mathbf{x}}(\circ), \tag{10}$$

where $\nabla_{\mathbf{x}}(\circ)$ is the spatial gradient (referred to the Cartesian system, $R_{\mathbf{x}}$) and $\mathbf{F}_{\boldsymbol{\chi}} = \frac{\partial\mathbf{x}}{\partial\boldsymbol{\chi}}$ is the convective deformation gradient, which measures the mesh distortion.

Defining the convective velocity as:

$$\mathbf{c}(\boldsymbol{\chi}, t) = \mathbf{F}_{\boldsymbol{\chi}} \cdot \mathbf{v}_{\boldsymbol{\chi}} = \mathbf{v}(\boldsymbol{\chi}, t) - \mathbf{v}_{mesh} \tag{11}$$

the material derivative within the ALE framework results in:

$$\left.\frac{D\phi}{Dt}\right|_{\boldsymbol{\chi}=\mathbf{X}} = \left.\frac{\partial\phi}{\partial t}\right|_{\boldsymbol{\chi}} + \mathbf{c}(\boldsymbol{\chi}, t) \cdot \nabla_{\mathbf{x}}(\phi) \tag{12}$$

Observe that $\mathbf{c}(\boldsymbol{\chi}, t)$ can be interpreted as the *relative* velocity of a particle with respect to the convective reference system, $R_{\boldsymbol{\chi}}$, which is moving with velocity, $\mathbf{v}_{mesh}$.

The spatial gradient in Eq. (12) is computed as $\nabla_{\mathbf{x}}(\circ) = \mathbf{F}^{-T} \cdot \nabla_{\mathbf{X}}(\circ)$, where $\nabla_{\mathbf{X}}(\circ)$ is the material gradient at the original configuration and $\mathbf{F} = \frac{\partial\mathbf{x}(\mathbf{X}, t)}{\partial\mathbf{X}}$ is the deformation gradient referred to the current position of the nodes of the mesh. This usually constitutes an added complexity in the ALE method because it is necessary to compute the movement of the mesh at each time-step (independently of the body motion). In many applications (e.g. forging analysis, CFD with moving free-surface, etc....) an ad hoc methodology is required to compute the position of the mesh at each time-step of the analysis.

However, when studying a FSW process, the mesh velocity can be prescribed according to the pin rotation as:

$$\mathbf{v}_{mesh}(\boldsymbol{\chi}, t) = \boldsymbol{\varpi} \times \mathbf{r}(\boldsymbol{\chi}, t), \tag{13}$$

where $\boldsymbol{\varpi}$ is the angular velocity of the pin and $\mathbf{r}(\boldsymbol{\chi}, t) = \boldsymbol{\chi}(t) - \mathbf{X}_o$ is the position of any grid point respect to the rotation axis, $\mathbf{X}_o$.

Therefore, it is possible to integrate Eq. (13) to compute the deformation gradient as: $\mathbf{F}_{\boldsymbol{\chi}} = \frac{\partial\mathbf{x}(\boldsymbol{\chi}, t)}{\partial\boldsymbol{\chi}} = \mathbf{R}$ where $\mathbf{R}(\boldsymbol{\varpi}, t)$ is a constant rotation tensor (we are assuming that $\mathbf{x}(\boldsymbol{\chi}, t) = \mathbf{R} \cdot \boldsymbol{\chi}(\mathbf{X}, t) + const.$).

3. Governing equations

In this section, the governing equations which define the thermo-mechanical problem are presented. The ALE framework is used

as it is the most general one, including both the Lagrangian and the Eulerian formulations as particular cases. Observe that this is very convenient from the programming point of view, leading to a unique format for all the balance equations. Table 1 summarizes the computational framework together with the solution hypotheses for the pin, the work-piece and the stir-zone.

3.1. Mechanical problem

The mechanical problem is defined by the momentum and mass conservation equations. The strong form of these balance equations in the ALE framework is:

$$\left.\frac{D\rho}{Dt}\right|_{\chi=\mathbf{X}} = \left.\frac{\partial\rho}{\partial t}\right|_{\chi} + \mathbf{c}\cdot\nabla_{\mathbf{x}}(\rho) = -\rho\nabla_{\mathbf{x}}\cdot\mathbf{v}, \tag{14}$$

$$\rho\left.\frac{D\mathbf{v}}{Dt}\right|_{\chi=\mathbf{X}} = \rho\left[\left.\frac{\partial\mathbf{v}}{\partial t}\right|_{\chi} + \mathbf{c}\cdot\nabla_{\mathbf{x}}(\mathbf{v})\right] = \nabla_{\mathbf{x}}\cdot\boldsymbol{\sigma} + \rho\mathbf{b}, \tag{15}$$

where $\boldsymbol{\sigma}(\chi,t)$ is the Cauchy stress tensor, $\mathbf{b}$ is the body force per unit of mass and $\nabla_{\mathbf{x}}\cdot(\circ)$ is the spatial divergence operator.

Modeling FSW process both Eqs. (14) and (15) can be simplified according to the following hypotheses:

- Strains are mainly deviatoric so that the volumetric deformations, including thermal effects, are neglected: material behavior is incompressible, $\rho = \rho_o$;
- The Reynolds number is very low, meaning that the inertia term can be neglected if compared to the viscous term;

The stress tensor can be split into volumetric and deviatoric parts as:

$$\boldsymbol{\sigma} = p\mathbf{I} + \mathbf{s}, \tag{16}$$

where $p = \frac{1}{3}\text{trace}(\boldsymbol{\sigma})$ is the pressure field and, $\mathbf{s}$, is the deviatoric stress tensor.

As a result the mechanical problem can be solved using the mixed ($\mathbf{v}/p$) quasi-static format of the balance of momentum equation together with the incompressibility (continuity) equation as:

$$\nabla\cdot\mathbf{s} + \nabla p + \rho_o\mathbf{b} = \mathbf{0}, \tag{17}$$

$$\nabla\cdot\mathbf{v} = 0, \tag{18}$$

where, for the sake of simplicity, the spatial divergence operator $\nabla_{\mathbf{x}}\cdot(\circ)$ is denoted (to the end of this work) simply by $\nabla\cdot(\circ)$.

3.2. Thermal problem

The strong form of the balance of energy equation in the ALE framework is:

$$\rho_o\left.\frac{De}{Dt}\right|_{\chi=\mathbf{X}} = \rho_o\left(\left.\frac{\partial e}{\partial t}\right|_{\chi} + \mathbf{c}\cdot\nabla e\right) = \boldsymbol{\sigma}:\dot{\boldsymbol{\varepsilon}} + \rho_o\,\dot{r} - \nabla\cdot\mathbf{q}, \tag{19}$$

where $e(\chi,t)$ is the specific internal energy, $\dot{r}$ is the rate of heat source per unit of mass and $\mathbf{q} = -k\nabla T$ is the heat flux, per unit of

surface, computed in terms of the temperature gradient, ∇T, and the thermal conductivity, k. The stress power, $\boldsymbol{\sigma}:\dot{\boldsymbol{\varepsilon}}$, is expressed in terms of the stress, $\boldsymbol{\sigma}$ and the strain rate, $\dot{\boldsymbol{\varepsilon}}$. Assuming the additive decomposition of the strain rate as:

$$\dot{\boldsymbol{\varepsilon}} = \dot{\boldsymbol{\varepsilon}}^e + \dot{\boldsymbol{\varepsilon}}^{vp}, \tag{20}$$

where $\dot{\boldsymbol{\varepsilon}}^e$ and $\dot{\boldsymbol{\varepsilon}}^{vp}$ are the elastic and visco-plastic parts, respectively, it is possible to rewrite Eq. (19) as:

$$\rho_o\left(\left.\frac{\partial h}{\partial t}\right|_{\chi} + \mathbf{c}\cdot\nabla h\right) = \dot{D}_{mech} + \rho_o\dot{r} - \nabla\cdot\mathbf{q}, \tag{21}$$

where $h(\chi,t)$ and D_{mech} are the specific enthalpy function and the mechanical dissipation, defined in rate format as:

$$\rho_o\dot{h} = \rho_o\,\dot{e} - \boldsymbol{\sigma}:\dot{\boldsymbol{\varepsilon}}^e, \tag{22}$$

$$\dot{D}_{mech} = \boldsymbol{\sigma}:\dot{\boldsymbol{\varepsilon}}^{vp} \geqslant 0. \tag{23}$$

It is common to express the enthalpy rate in terms of the temperature rate as:

$$\rho_o\dot{h} = \rho_o c\dot{T}, \tag{24}$$

where c is the specific heat capacity. This given, the balance of energy equation can be rewritten as:

$$\rho_o c\left(\left.\frac{\partial T}{\partial t}\right|_{\chi} + \mathbf{c}\cdot\nabla T\right) = \dot{D}_{mech} + \rho_o\dot{r} - \nabla\cdot\mathbf{q} \tag{25}$$

which is the *heat transfer equation* for a continuum body in the ALE format.

3.3. Local form of the FSW problem

The FSW problem is stated by coupling the quasi-static mechanical governing Eqs. (17) and (18) with the transient heat transfer equation in (25):

$$\begin{cases} \nabla\cdot\mathbf{s} + \nabla p + \rho_o\,\mathbf{b} = \mathbf{0}, \\ \nabla\cdot\mathbf{v} = 0, \\ \rho_o c\left(\left.\frac{\partial T}{\partial t}\right|_{\chi} + \mathbf{c}\cdot\nabla T\right) = \dot{D}_{mech} - \nabla\cdot\mathbf{q} \end{cases} \tag{26}$$

where the volumetric heat source, $\rho_o\,\dot{r}$, is generally neglected in FSW analysis.

Eqs. (26) state the equilibrium for both the mechanical and the thermal problems in *local form*, that is, at each point, $\chi(t)$, of the integration domains defined in R_χ. Therefore, it is interesting to observe that in the pin domain, all the state variables, $\mathbf{v}, p$ and T, as well as any derived variable, such as $\mathbf{s}(\mathbf{v},T)$ or $\mathbf{q}(T)$, are referred to a material particle, $\mathbf{X}$, while in the work-piece, they are referred to a spatial point, $\mathbf{x}$ in the Cartesian domain $R_\mathbf{x}$ (see Table 2).

3.4. Mechanical constitutive laws

The FSW process is characterized by high strain rates as well as by a wide temperature range from the environment temperature

Table 1
Convective velocity, material derivative and spatial gradient in Lagrangian (pin), Eulerian (work-piece) and ALE (stir-zone) formulations.

Pin	Work-piece	Stir-zone
Lagrangian	Eulerian	ALE
$\chi = \mathbf{X}$	$\chi = \mathbf{x}$	$\chi \neq \mathbf{X} \neq \mathbf{x}$
$\mathbf{v}_{mesh} = \mathbf{v}$	$\mathbf{v}_{mesh} = \mathbf{0}$	$\mathbf{v}_{mesh} = \boldsymbol{\varpi}\times\mathbf{r}$
$\mathbf{c} = \mathbf{0}$	$\mathbf{c} = \mathbf{v}$	$\mathbf{c} = \mathbf{v} - \mathbf{v}_{mesh}$
$\left.\frac{D(\circ)}{Dt}\right|_{\chi=\mathbf{X}} = \left.\frac{\partial(\circ)}{\partial t}\right|_{\mathbf{X}}$	$\left.\frac{D(\circ)}{Dt}\right|_{\chi=\mathbf{X}} = \left.\frac{\partial(\circ)}{\partial t}\right|_{\mathbf{x}} + \mathbf{v}\cdot\nabla_{\mathbf{x}}(\circ)$	$\left.\frac{D(\circ)}{Dt}\right|_{\chi=\mathbf{X}} = \left.\frac{\partial(\circ)}{\partial t}\right|_{\chi} + \mathbf{c}\cdot\nabla_{\mathbf{x}}(\circ)$
$\nabla_{\mathbf{x}}(\circ) = \mathbf{F}^{-T}\cdot\nabla_{\mathbf{X}}(\circ)$	$\nabla_{\mathbf{x}}(\circ) = \nabla_{\mathbf{X}}(\circ)$	$\nabla_{\mathbf{x}}(\circ) = \mathbf{F}^{-T}\cdot\nabla_{\mathbf{X}}(\circ)$

Table 2
Velocity, temperature, heat flux and stress fields in Lagrangian (pin), Eulerian (work-piece) and ALE (stir-zone) formulations.

Pin	Work-piece	Stir-zone
Lagrangian	Eulerian	ALE
$\chi = \mathbf{X}$	$\chi = \mathbf{x}$	$\chi \neq \mathbf{X} \neq \mathbf{x}$
$\mathbf{v}(\mathbf{X},t)$	$\mathbf{v}(\mathbf{x},t)$	$\mathbf{v}(\chi,t)$
$T(\mathbf{X},t)$	$T(\mathbf{x},t)$	$T(\chi,t)$
$\boldsymbol{\sigma}(\mathbf{X},t)$	$\boldsymbol{\sigma}(\mathbf{x},t)$	$\boldsymbol{\sigma}(\chi,t)$
$\mathbf{q}(\mathbf{X},t)$	$\mathbf{q}(\mathbf{x},t)$	$\mathbf{q}(\chi,t)$

to the melting point. Hence, the constitutive laws to be adopted for the work-piece and, particularly, in the stir-zone should be dependent on both variables. The pin needs not be included in the following discussion because its corresponding constitutive equations (in Lagrangian format) are usually defined by a simple thermo-elastic or thermo-rigid law.

According to the split of the stress tensor introduced in (16), it is common [60,61,67] to adopt a *rigid visco-plastic* behavior, using a rate-dependent constitutive law expressed as:

$$\mathbf{s} = 2\mu_{eff}\dot{\mathbf{e}}, \tag{27}$$

where μ_{eff} is the effective viscosity of the material and $\dot{\mathbf{e}} = \mathrm{dev}(\dot{\boldsymbol{\varepsilon}})$ is the deviatoric part of the total strain rate, $\dot{\boldsymbol{\varepsilon}}$ which is computed as:

$$\dot{\boldsymbol{\varepsilon}} = \nabla^s \mathbf{v}, \tag{28}$$

where $\nabla^s \mathbf{v}(\circ)$ denotes the symmetric spatial gradient operator. In FSW, the elastic part of the strain tensor, $\dot{\boldsymbol{\varepsilon}}^e$, in (20) is negligible if compared with the visco-plastic component, $\dot{\boldsymbol{\varepsilon}}^{vp}$, so that:

$$\dot{\boldsymbol{\varepsilon}} \equiv \dot{\boldsymbol{\varepsilon}}^{vp} \tag{29}$$

and all the deformation is assumed to be visco-plastic. Furthermore, it is also common to neglect the volumetric deformation, so that the total strain rate is purely deviatoric:

$$\dot{\boldsymbol{\varepsilon}} \equiv \mathrm{dev}(\dot{\boldsymbol{\varepsilon}}) = \dot{\mathbf{e}}. \tag{30}$$

This incompressible behavior of the material requires a special treatment from the computational point of view.

With regard to the definition of the effective viscosity, μ_{eff}, different constitutive characterizations can be adopted. A first choice is the classical Norton–Hoff model [53,46], which assumes that the effective viscosity is a function of the temperature and the equivalent plastic strain-rate, $\dot{\varepsilon}_{eq} = \sqrt{\frac{2}{3}}\|\dot{\boldsymbol{\varepsilon}}\| = \sqrt{\frac{2}{3}(\dot{\boldsymbol{\varepsilon}} : \dot{\boldsymbol{\varepsilon}})}$, in the form:

$$\mu_{eff}(\dot{\varepsilon}_{eq}, T) = \mu\left(\sqrt{3}\dot{\varepsilon}_{eq}\right)^{m-1}, \tag{31}$$

where $\mu(T)$ and $0 \leqslant m(T) \leqslant 1$ are the (temperature dependent) viscosity and the (temperature dependent) rate-sensitivity parameters, respectively. The linear case $m = 1$ recovers the Newtonian behavior:

$$\mathbf{s} = 2\mu\dot{\mathbf{e}} \tag{32}$$

with a linear relationship between stresses and strain-rates. Rigid perfect-plastic behavior corresponds to $m = 0$:

$$\mathbf{s} = \sqrt{2}\mu\,\mathbf{n}, \tag{33}$$

where $\mathbf{n} = \frac{\dot{\mathbf{e}}}{\|\dot{\mathbf{e}}\|} = \frac{\mathbf{s}}{\|\mathbf{s}\|}$ defines the plastic-flow direction.

In FSW, the rate-sensitivity parameter is usually in the range $0.1 \leqslant m \leqslant 0.3$ with a very non-linear (non-Newtonian) behavior.

An alternative to the Norton–Hoff model is the Sheppard–Wright model [62]. In this case, the effective viscosity, $\mu_{eff}(\dot{\varepsilon}_{eq}, T)$ is a function of the equivalent plastic strain-rate and the temperature field in the following form:

$$\mu_{eff}(\dot{\varepsilon}_{eq}, T) = \frac{1}{3}\frac{\sigma_{eff}}{\dot{\varepsilon}_{eq}}, \tag{34}$$

where the effective stress $\sigma_{eff}(\dot{\varepsilon}_{eq}, T)$ is defined as [67]:

$$\sigma_{eff}(\dot{\varepsilon}_{eq}, T) = \frac{1}{\alpha}\sinh^{-1}\left[\left(\frac{Z}{A}\right)^{\frac{1}{n}}\right] = \frac{1}{\alpha}\ln\left[\left(\frac{Z}{A}\right)^{\frac{1}{n}} + \sqrt{1 + \left(\frac{Z}{A}\right)^{\frac{2}{n}}}\right] \tag{35}$$

being α, A and n material constants. The Zener–Hollomon parameter, $Z = \dot{\varepsilon}_{eq}\exp\left(\frac{Q}{RT_k}\right)$ takes into account the temperature dependency ($T_k = T + 273.16$ is the absolute temperature), Q is the activation energy and finally, R is the universal gas constant.

The final step required to the constitutive model is to compute the plastic (stirring) dissipation, which is one of the key mechanisms of heat generation during the welding process together with the friction dissipation. The plastic dissipation rate, $\dot{D}_{mech}$, is computed for both constitutive models as:

$$\dot{D}_{mech} = \boldsymbol{\sigma} : \dot{\boldsymbol{\varepsilon}}^{vp} = \mathbf{s} : \dot{\mathbf{e}} = 2\mu_{eff}\|\dot{\boldsymbol{\varepsilon}}\|^2 = \sigma_{eff}\dot{\varepsilon}_{eq}. \tag{36}$$

- *Remark-1*: The advantage of the Sheppard–Wright model is the possibility of a better calibration of the material behavior in the entire temperature range from the environment temperature to the melting point while in Norton–Hoff model the temperature dependency must be introduced by means of a tabulated (temperature dependent) viscosity.
- *Remark-2*: Neither the Sheppard–Wright nor the Norton–Hoff models take into account the thermo-elastic strains. This means that the proposed constitutive laws are not able to predict the residual stresses after joining and cooling back to room temperature. The study of the residual stresses is more appropriate at global level simulation where the full part/structure is studied using a Lagrangian formulation and a moving heat source computed in a locally based FSW simulation (scope of the present paper).
- *Remark-3*: The proposed formulation could incorporate a more sophisticated strain-based mechanical model able to account for the thermal softening as proposed in [44,57,9]. To this end, the integration of the strain variables along the stream-lines would be necessary.

4. Time integration

The numerical solution of the coupled thermo-mechanical problem (26) involves the transformation of an infinite dimensional transient system into a sequence of discrete non-linear algebraic problems. This can be achieved by means of a time-marching scheme for the advancement of the primary nodal variables, velocities, pressure and temperatures, together with a return mapping algorithm to update the internal variables.

With regard to the time stepping scheme different strategies are possible, but they can be grouped in two categories: simultaneous (monolithic) solutions and staggered (block-iterative or fractional-step) time-stepping algorithms. In this work, a staggered solution is adopted. A product formula algorithm is introduced, leading to a time-integration scheme in which the two sub-problems (thermal and mechanical) are solved sequentially, within the framework of the classical fractional step methods (see [3,15]).

Let us consider the following (homogeneous) first order constrained dissipative local problem of evolution [24]:

$$\begin{aligned} \dot{\mathbf{Z}} &= \mathbf{A}(\mathbf{Z}) \quad \text{in} \quad \Omega_\chi \times [0, t], \\ \mathbf{Z}(t_o) &= \mathbf{Z}_o \quad \text{in} \quad \Omega_\chi, \end{aligned} \tag{37}$$

where $\mathbf{Z} = [\rho, \mathbf{v}, h]^T$ is the set of primary independent variables and $\mathbf{A}(\mathbf{Z})$ is a non-linear operator defined as:

$$\mathbf{A}(\mathbf{Z}) = \begin{cases} -\rho\nabla \cdot \mathbf{v}, \\ \frac{1}{\rho}(\nabla \cdot \mathbf{s} + \nabla p + \rho\mathbf{b}), \\ \frac{1}{\rho}\left(\dot{D}_{mech} - \nabla \cdot \mathbf{q}\right). \end{cases} \tag{38}$$

For quasi-static incompressible problems, $\dot{\mathbf{Z}} = \left[0, \mathbf{0}, \dot{h}\right]^T$, and the general operator (38) can be replaced by:

$$\mathbf{A}(\mathbf{Z}) = \begin{cases} \nabla \cdot \mathbf{v}, \\ \frac{1}{\rho_o}(\nabla \cdot \mathbf{s} + \nabla p + \rho_o\mathbf{b}), \\ \frac{1}{\rho_o}\left(\dot{D}_{mech} - \nabla \cdot \mathbf{q}\right). \end{cases} \tag{39}$$

The fractional step method is based on an additive *isothermal* operator split of the differential operator $\mathbf{A}(\mathbf{Z})$ of the form [6,7,4]:

$$\mathbf{A}(\cdot) = A_{mech}^{(1)}(\mathbf{Z}) + \mathbf{A}_{ther}^{(2)}(\mathbf{Z}), \tag{40}$$

where the operators $\mathbf{A}_{mech}^{(1)}(\mathbf{Z})$ and $\mathbf{A}_{ther}^{(2)}(\mathbf{Z})$ are defined as:

$$\mathbf{A}_{mech}^{(1)}(\mathbf{Z}) = \begin{cases} \nabla \cdot \mathbf{v}, \\ \frac{1}{\rho_o}(\nabla \cdot \mathbf{s} + \nabla p + \rho_o \mathbf{b}). \\ 0, \end{cases} \tag{41}$$

$$\mathbf{A}_{ther}^{(2)}(\mathbf{Z}) = \begin{cases} 0, \\ \mathbf{0}. \\ \frac{1}{\rho_o}\left(\dot{D}_{mech} - \nabla \cdot \mathbf{q}\right). \end{cases} \tag{42}$$

The solution $\mathbf{Z}_{n+1}$ at time t_{n+1} is obtained in two steps: firstly, the mechanical sub-problem defined by $\mathbf{A}_{mech}^{(1)}(\mathbf{Z})$ is solved starting from the solution $\mathbf{Z}_n$ at time t_n. The result is an *intermediate* solution $\overline{\mathbf{Z}}_{n+1}$, used as starting point for the thermal sub-problem $\mathbf{A}_{ther}^{(2)}(\mathbf{Z})$:

Sub – problem 1

$$\mathbf{Z}_n \rightarrow \dot{\mathbf{Z}} = \mathbf{A}_{mech}^{(1)}(\mathbf{Z}) \rightarrow \overline{\mathbf{Z}}_{n+1}, \tag{43}$$

Sub – problem 2

$$\overline{\mathbf{Z}}_{n+1} \rightarrow \dot{\mathbf{Z}} = \mathbf{A}_{ther}^{(2)}(\mathbf{Z}) \rightarrow \mathbf{Z}_{n+1}. \tag{44}$$

Sub-problem 1 defines a mechanical phase at fixed enthalpy (temperature) and *Sub-problem 2* defines a thermal phase at fixed configuration. As a result, the original coupled problem is split into two smaller partitions, allowing the use of any integration technique originally developed for the uncoupled sub-problems.

The algorithm presented above is *first order* accurate, and it does not require an iteration loop over the two problems within the same time-step. It is worth to point out that the split (39) is formulated for the continuum operator $\mathbf{A}$ and not for the discrete operator, say $\mathbf{A}^h$, arising from a spatial discretization of the initial-boundary value problem. If the split is performed for the discrete operator $\mathbf{A}^h$, the classical Jacobi and Gauss–Seidel iterative methods arise.

The critical restriction to guarantee *stability* when using the operator split (39) is that each one of the sub-problems must preserve the dissipative structure of the original problem, that is:

$$\int_{\Omega_\chi} \dot{D}_{int}^{(\alpha)}(\mathbf{Z}^{(\alpha)}) \, dV = \int_{\Omega_\chi} \left[\dot{D}_{mech}^{(\alpha)}(\mathbf{Z}^{(\alpha)}) + \dot{D}_{cond}^{(\alpha)}(\mathbf{Z}^{(\alpha)}) \right] dV \geqslant 0, \tag{45}$$

$$\alpha = 1, 2,$$

where $\mathbf{Z}^{(\alpha)}$ denotes the solution obtained by each operator $\mathbf{A}^{(\alpha)}(\mathbf{Z}^{(\alpha)})$, $\alpha = 1, 2$. Restriction (45) is directly related to the satisfaction of the *second principle of the thermodynamics*, where the internal dissipation $\dot{D}_{int}$ is split into mechanical dissipation and dissipation by conduction, $\dot{D}_{mech}$ and $\dot{D}_{cond}$, respectively. In this work, due to the particular form of the constitutive equations adopted for the FSW process, $\dot{D}_{mech}$ and $\dot{D}_{cond}$ are always non-negative in both sub-problems:

$$\dot{D}_{mech} = \boldsymbol{\sigma} : \dot{\boldsymbol{\varepsilon}}^{vp} = 2\mu_{eff} \|\dot{\boldsymbol{\varepsilon}}\|^2 \geqslant 0 \leftarrow \mu_{eff} > 0, \tag{46}$$

$$\dot{D}_{cond} = -\frac{\mathbf{q} \cdot \nabla T}{T} = \frac{k\|\nabla T\|^2}{T} \geqslant 0 \leftarrow k > 0. \tag{47}$$

The final result is an accurate, efficient and robust numerical strategy for the numerical simulation of coupled thermo-mechanical problems such as the FSW processes.

5. Weak form of the coupled problem

Let us denote by Ω_χ an open and bounded domain in $\mathbb{R}^{n_{dim}}$ where n_{dim} is the number of dimensions of the space, and $\partial\Omega_\chi$ its boundary. Let us assume that the boundary $\partial\Omega_\chi$ can be split into $\partial\Omega_\sigma$ and $\partial\Omega_v$, being $\partial\Omega_\chi = \partial\Omega_\sigma \cup \partial\Omega_v$ such that tractions are prescribed on $\partial\Omega_\sigma$ while velocities are specified on $\partial\Omega_v$, respectively. In a similar way, boundary $\partial\Omega_\chi$ can be also split into $\partial\Omega_q$ and $\partial\Omega_\theta$ such that $\partial\Omega_\chi = \partial\Omega_q \cup \partial\Omega_\theta$, where fluxes (on $\partial\Omega_q$) and temperatures (on $\partial\Omega_\theta$) are prescribed for the heat transfer analysis.

In the FSW problem, the integration domain $\Omega_\chi = \Omega(\boldsymbol{\chi}(t))$ is subdivided into three different regions corresponding to the pin, the work-piece and the stir-zone, as previously discussed. Let us recall that when studying the work-piece, the integration domain, $\Omega_\chi = \Omega(\mathbf{x})$, does not move: it is defined in the Cartesian (Eulerian) space. The integration domain of the pin, $\Omega_\chi(t) = \Omega(\mathbf{X}, t)$, moves according to the displacement field of the material particles, $\mathbf{u}(\mathbf{X}, t)$. Finally, the mesh defined for the stir-zone, $\Omega_\chi(t) = \Omega(\boldsymbol{\chi}(t))$, moves but the mesh velocity $\mathbf{v}_{mesh}(\boldsymbol{\chi}(t))$, is different from the material velocity, $\mathbf{v}(\mathbf{X}, t)$.

The weak form of the mechanical sub-problem defined in (43) is:

$$\begin{cases} \int_{\Omega_\chi}[(\nabla \cdot \mathbf{s}) \cdot \delta\mathbf{v}]dV + \int_{\Omega_\chi}(\nabla p \cdot \delta\mathbf{v})\,dV + \int_{\Omega_\chi}(\rho_o \mathbf{b} \cdot \delta\mathbf{v})dV = 0 & \forall \delta\mathbf{v}, \\ \int_{\Omega_\chi}[(\nabla \cdot \mathbf{v})\delta p]\,dV = 0 & \forall \delta p \end{cases} \tag{48}$$

and the thermal sub-problem defined in (44) results in:

$$\int_{\Omega_\chi}\left[\rho_o c\left(\left.\frac{\partial T}{\partial t}\right|_\chi + \mathbf{c} \cdot \nabla T\right)\delta T\right]dV + \int_{\Omega_\chi}[(\nabla \cdot \mathbf{q})\delta T]\,dV$$
$$- \int_{\Omega_\chi}\left(\dot{D}_{mech}\delta T\right)dV = 0 \quad \forall \delta T, \tag{49}$$

where $\delta\mathbf{v}$, δp and δT are the variations compatible with the Dirichlet boundary conditions (test functions) of velocity, pressure and temperature fields, respectively.

Integrating by parts, the following expressions are obtained:

$$\int_{\Omega_\chi}[(\nabla \cdot \mathbf{s}) \cdot \delta\mathbf{v}]dV = -\int_{\Omega_\chi}(\mathbf{s} : \nabla^s \delta\mathbf{v})dV + \int_{\partial\Omega_\sigma}(\bar{\mathbf{t}} \cdot \delta\mathbf{v})dS, \tag{50}$$

$$\int_{\Omega_\chi}(\nabla p \cdot \delta\mathbf{v})\,dV = -\int_{\Omega_\chi}(p\nabla \cdot \delta\mathbf{v})\,dV, \tag{51}$$

$$\int_{\Omega_\chi}[(\nabla \cdot \mathbf{q})\delta T]dV = -\int_{\Omega_\chi}\mathbf{q} \cdot \nabla(\delta T)\,dV - \int_{\partial\Omega_q}(\bar{q}\,\delta T)dS, \tag{52}$$

where $\bar{\mathbf{t}} = \boldsymbol{\sigma} \cdot \mathbf{n}$ are prescribed tractions on $\partial\Omega_\sigma$, while $\bar{q} = -\mathbf{q} \cdot \mathbf{n}$ are prescribed heat fluxes on $\partial\Omega_q$.

Substituting (50) and (51) in (48), the mixed $(\mathbf{v}/p)$ variational form of the quasi-static incompressible mechanical problem yields:

$$\begin{cases} \int_{\Omega_\chi}(\mathbf{s} : \nabla^s \delta\mathbf{v})dV + \int_{\Omega_\chi}(p\,\nabla \cdot \delta\mathbf{v})\,dV = W_{mech}^{ext} & \forall \delta\mathbf{v}, \\ \int_{\Omega_\chi}[(\nabla \cdot \mathbf{v})\delta p]\,dV = 0 & \forall \delta p, \end{cases} \tag{53}$$

and, in a similar way, substituting (52) in (49), the variational form of the transient thermal problem results in:

$$\int_{\Omega_\chi}\left[\rho_o c\left(\left.\frac{\partial T}{\partial t}\right|_\chi + \mathbf{c} \cdot \nabla T\right)\delta T\right]dV + \int_{\Omega_\chi}k\nabla T \cdot \nabla(\delta T)\,dV = W_{ther}^{ext} \quad \forall \delta T, \tag{54}$$

where the heat flux has been computed using the Fourier's law: $\mathbf{q} = -k\nabla T$, being, k, the thermal conductivity.

In Eqs. (53) and (54), W_{mech}^{ext} and W_{ther}^{ext} denote the external work of the mechanical and thermal loads, respectively:

$$W_{mech}^{ext}(\delta\mathbf{v}) = \int_{\Omega_\chi}(\rho_o \mathbf{b} \cdot \delta\mathbf{v})dV + \int_{\partial\Omega_\sigma}(\bar{\mathbf{t}} \cdot \delta\mathbf{v})dS, \tag{55}$$

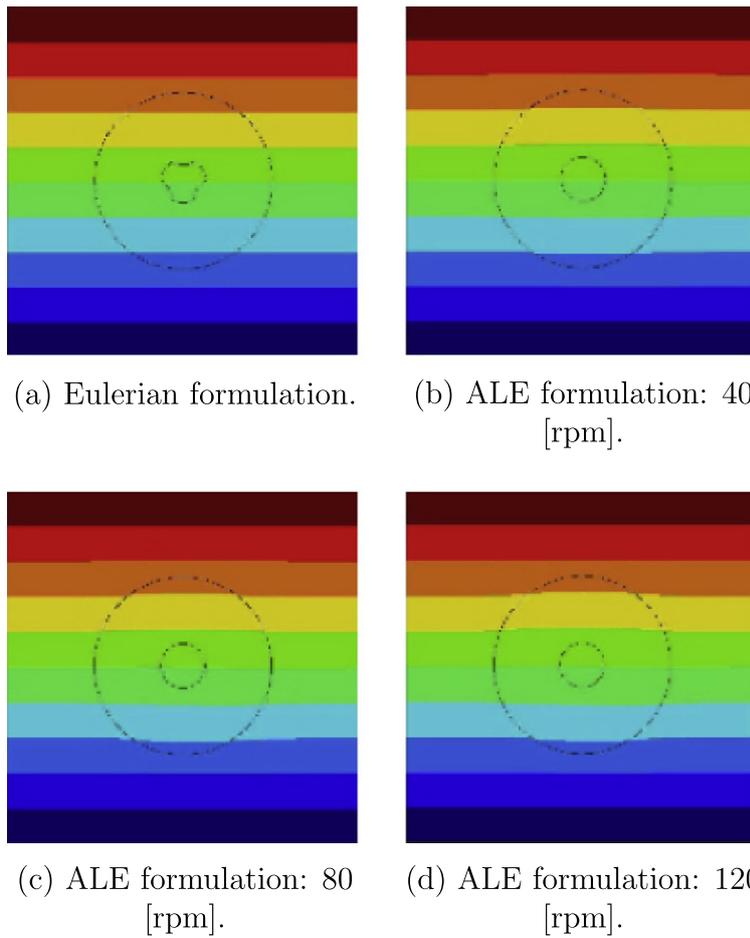$$W_{ther}^{ext}(\delta T) = \int_{\Omega_\chi}\left(\dot{D}_{mech}\delta T\right)dV + \int_{\partial\Omega_q}(\bar{q}\delta T)dS. \tag{56}$$
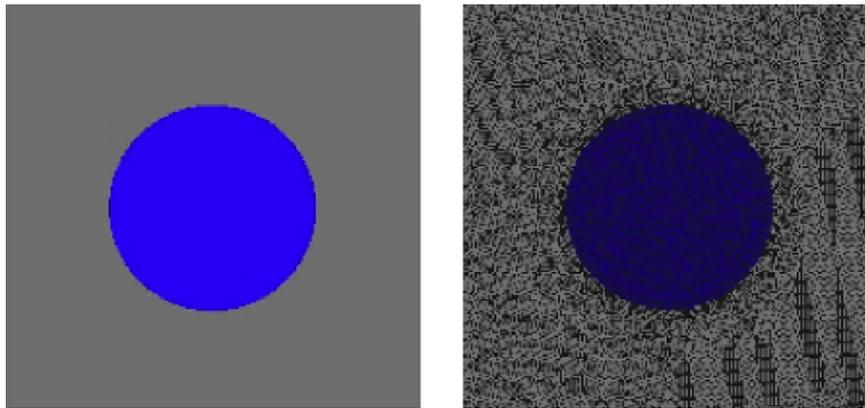
(a) Geometry: Eulerian domain (gray) and ALE domain (blue).

(b) FE mesh.

Fig. 2. ALE formulation benchmarking: geometry and FE mesh.

(a) Eulerian formulation.

(b) ALE formulation: 40 [rpm].

(c) ALE formulation: 80 [rpm].

(d) ALE formulation: 120 [rpm].

Fig. 3. ALE formulation bechmarking: temperature field after one revolution.

The coupled problem defined by the variational forms in (53) and (54) is subjected to appropriate Dirichlet boundary conditions in terms of prescribed velocity and temperature field, $\mathbf{v} = \bar{\mathbf{v}}$ and $T = \bar{T}$ in $\partial\Omega_v$ and $\partial\Omega_\theta$, respectively, and the initial conditions for the transient thermal problem in terms of initial temperature field: $T(t = 0) = T_o$.

Table 3
Time-step used in the numerical simulations according to the different angular velocities.

rpm	Period [s]	Δt [s]
40	1.50	5.791×10^{-3}
80	0.75	2.988×10^{-3}
120	0.50	1.992×10^{-3}

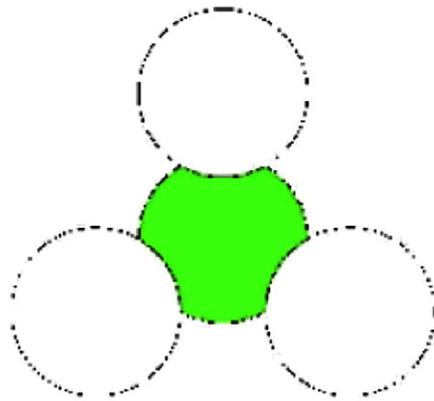### 5.1. Discrete and stabilized weak form of the mechanical problem

In the framework of the standard Galerkin finite element method, the discrete counterpart of the weak form for the mechanical problem (53) can be written as:

$$\begin{cases} \int_{\Omega_\chi} (\mathbf{s}_h : \nabla^s \delta\mathbf{v}_h) dV + \int_{\Omega_\chi} (p_h \ \nabla \cdot \delta\mathbf{v}_h) dV = W_{mech}^{ext}(\delta\mathbf{v}_h) & \forall \delta\mathbf{v}_h, \\ \int_{\Omega_\chi} [(\nabla \cdot \mathbf{v}_h)\delta p_h] \ dV = 0 & \forall \delta p_h, \end{cases}$$

(57)

where $\mathbf{v}_h, \delta\mathbf{v}_h \in S_h$ and $p_h, \delta p_h \in P_h$ are the finite element approximations and the corresponding variations of the velocity and pressure fields, respectively, within the finite element spaces: $S_h \subset H^1(\Omega_\chi)$ and $P_h \subset L^2(\Omega_\chi)$. The Ladyzhenskaya–Babuška–Brezzi (LBB) compatibility condition [14] restricts the choice of the finite element spaces S_h and P_h to guarantee the stability of the solution. For instance, standard Galerkin mixed ($P1P1$) elements with continuous equal order linear $\mathbf{v}/p$ interpolation violate the LBB condition; this produces instabilities in the pressure field and poor numerical performance. Stability can be achieved either choosing $\mathbf{v}/p$ interpolation spaces that satisfy the LBB condition (e.g. $P2P1$ elements) or, alternatively, circumventing this condition. A possible choice consists of using a stabilization technique within the framework of the *variational multi scale* (VMS) method (see the original idea in [48]). In our work, the *orthogonal subgrid scale* (OSS) stabilization technique has been adopted to stabilize $P1P1$ mixed $\mathbf{v}/p$ elements with continuous equal order linear interpolation. The OSS technique, originally developed to fulfill the incompressibility condition in CFD problems (see [26,28,27]), has been exploited in the solid mechanics context to deal with elastic incompressibility and J2-plasticity (isochoric) problems (see [5,17,21,22,54]). The resulting discrete OSS stabilized weak form of the mechanical problem results in:
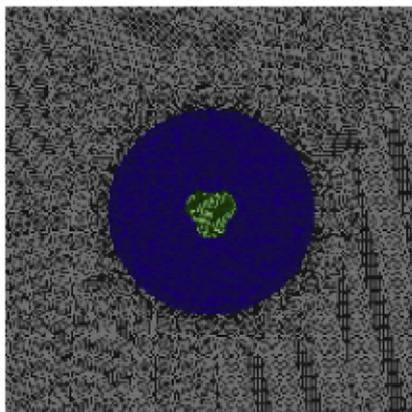
$$\begin{cases} \int_{\Omega_\chi} (\mathbf{s}_h : \nabla^s \delta\mathbf{v}_h) dV + \int_{\Omega_\chi} (p_h \nabla \cdot \delta\mathbf{v}_h) dV = W_{mech}^{ext}(\delta\mathbf{v}_h) & \forall \delta\mathbf{v}_h, \\ \int_{\Omega_\chi} [(\nabla \cdot \mathbf{v}_h)\delta p_h] \, dV - \int_{\Omega_\chi} \tau_u[\nabla\delta p_h \cdot (\nabla p_h - \mathbf{\Pi}_h)] dV = 0 & \forall \delta p_h, \\ \int_{\Omega_\chi} (\nabla p_h \cdot \delta\mathbf{\Pi}_h) dV - \int_{\Omega_\chi} (\mathbf{\Pi}_h \cdot \delta\mathbf{\Pi}_h) dV = 0 & \forall \delta\mathbf{\Pi}_h, \end{cases}$$
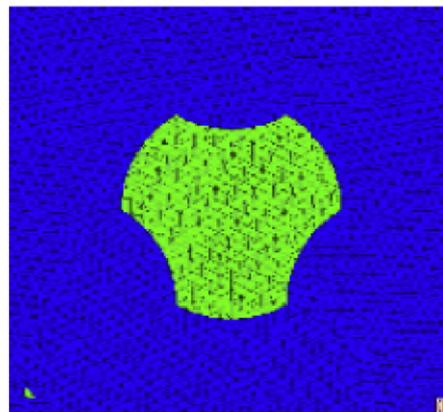
(58)

(a) Triflute pin design.
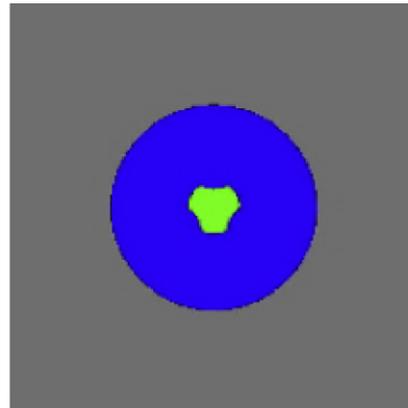
(b) Work-piece (gray), stir-zone (blue) and pin (green).

(c) FE mesh.

(d) Detail of the FE mesh.

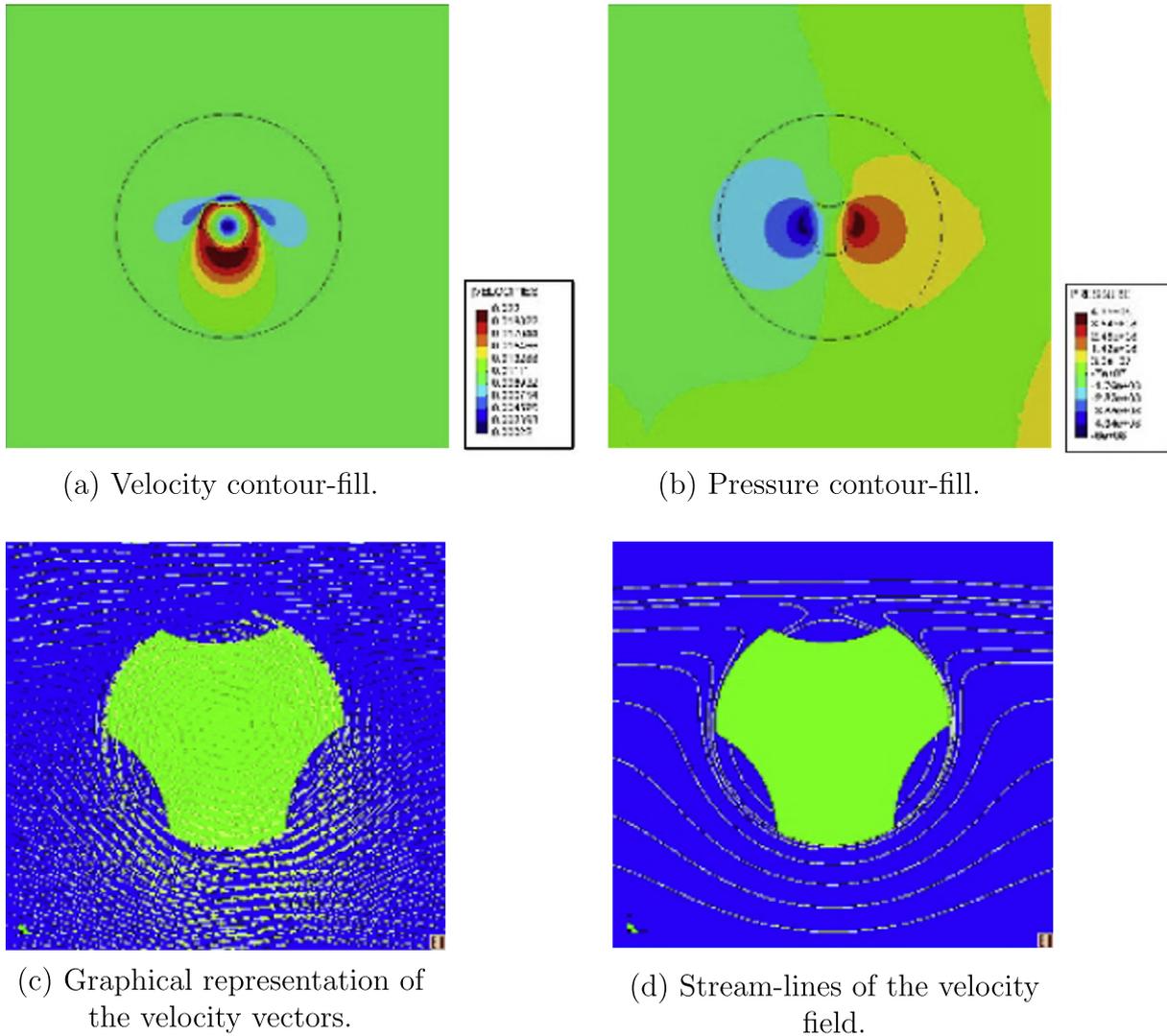**Fig. 4.** Triflute pin FSW analysis: geometry and FE mesh.

(a) Velocity contour-fill.

(b) Pressure contour-fill.

(c) Graphical representation of the velocity vectors.

(d) Stream-lines of the velocity field.

Fig. 5. FSW analysis using a triflute pin.

where $\mathbf{\Pi}_h$ and $\delta\mathbf{\Pi}_h$ are the smooth projection of the pressure gradient onto the finite element space and its variation.

The stabilization term introduced in the second Eq. of (58) is computed as a function of the orthogonal projection of the residual of the momentum balance equation (see first Eq. in (26)) as:

$$P^{\perp}(\nabla p_h) = \nabla p_h - \mathbf{\Pi}_h,$$

where the orthogonal projection of $\nabla \cdot \mathbf{s}$ vanishes when using linear triangles or tetrahedral elements. The stabilization parameter, τ_u, is computed element by element as:

$$\tau_u = c_u \frac{h_e^2}{2\mu_{eff}}, \tag{59}$$

where h_e is the element size, c_u is a constant and μ_{eff} is the effective viscosity. Observe that the effective viscosity $\mu_{eff}(T)$ is (usually) a temperature dependent parameter leading to a temperature dependent definition of the stabilization parameter, $\tau_u(T)$.

The resulting system in (58) is an accurate, stable and consistent (as the stabilization term vanishes on mesh refinement) formulation to solve the mechanical problem subjected to the incompressibility constraint.

5.2. Discrete and stabilized weak form of the thermal problem

The discrete counterpart of the weak form for the thermal problem (56) is written as:

$$\int_{\Omega_\chi} \left[\rho_o c \left(\frac{\partial T_h}{\partial t}\bigg|_\chi + \mathbf{c}_h \cdot \nabla T_h \right) \delta T_h \right] dV + \int_{\Omega_\chi} k \nabla T_h \cdot \nabla(\delta T_h)\, dV$$
$$= W_{ther}^{ext}(\delta T_h) \qquad\qquad \forall \delta T_h, \tag{60}$$

where $(T_h, \delta T_h) \in \Theta_h$ are the finite element approximations and the corresponding variations of the temperature field within the finite element space $\Theta_h \subset H^1(\Omega_\chi)$. Here, the stability problems may arise due to the convective term. Also in this case, it is possible to adopt the VMS framework to stabilize the formulation adding a residual-based OSS stabilization term of the form:

$$\text{Stab}(\delta T_h) = \int_{\Omega_\chi} \tau_\theta \rho_o c \left[\mathbf{c}_h \cdot \nabla(\delta T_h) (\mathbf{c}_h \cdot \nabla T_h - \Pi_h^\theta) \right] dV, \tag{61}$$

where $\tau_\theta = c_\theta \frac{h_e}{2\|\mathbf{c}_h\|}$ is the stabilization parameter for the thermal (convective) problem, c_θ is a constant and Π_h^θ is the smooth projection of the convective term given by:

$$\int_{\Omega_\chi} \left[(\mathbf{c}_h \cdot \nabla T_h) \delta \Pi_h^\theta \right] dV - \int_{\Omega_\chi} (\Pi_h^\theta \cdot \delta \Pi_h^\theta) dV = 0 \quad \forall \delta \Pi_h^\theta. \tag{62}$$

(a) After 1 revolution.

(b) After 4 revolutions.

(c) After 7 revolutions.

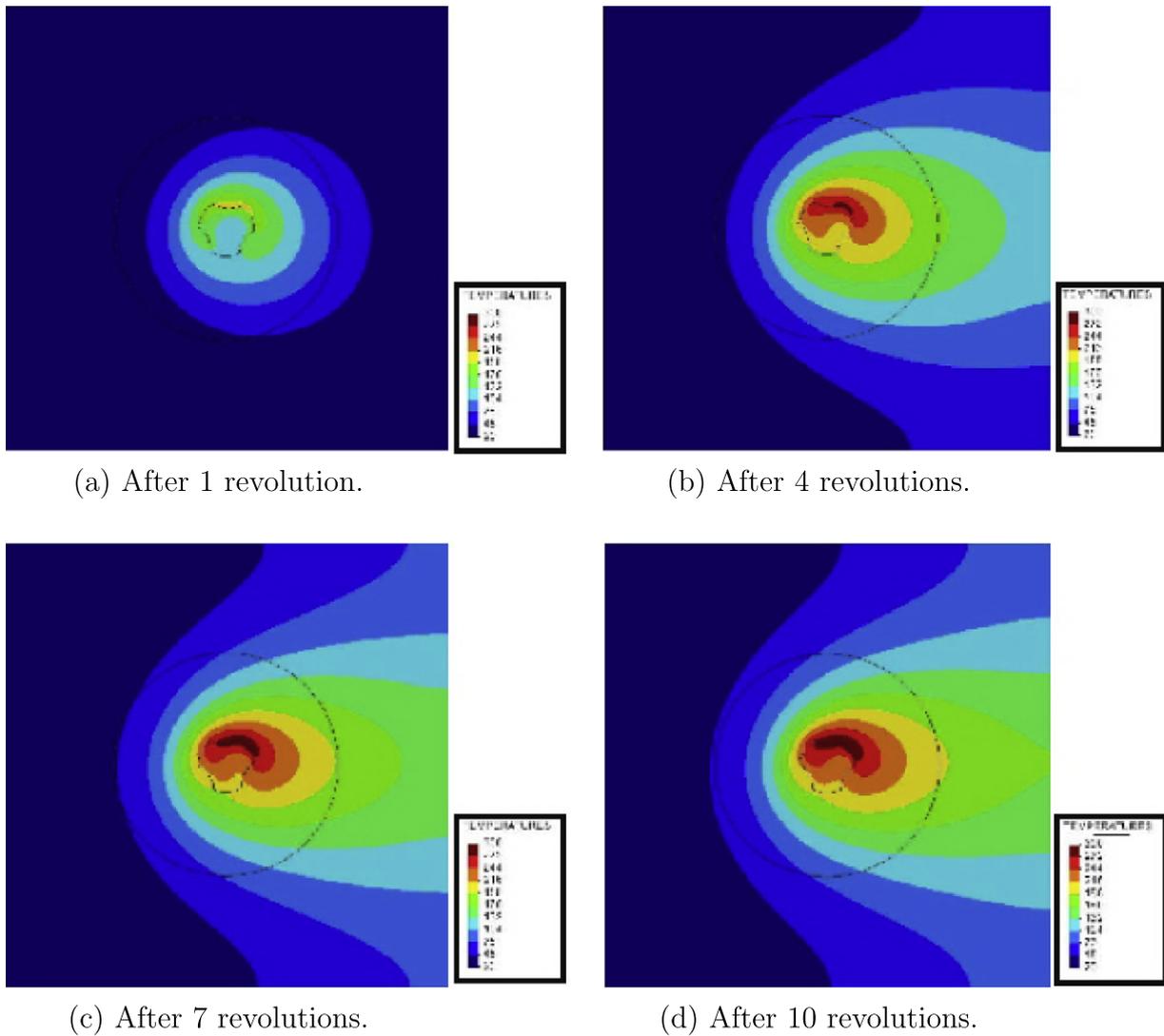

(d) After 10 revolutions.

Fig. 6. FSW analysis using a triflute pin: temperature evolution [°C].

The resulting discrete OSS stabilized weak form of the thermal problem is:

$$
\begin{cases}
\int_{\Omega_\chi} \left[\rho_o c \left(\left. \frac{\partial T_h}{\partial t} \right|_\chi + \mathbf{c}_h \cdot \nabla T_h \right) \delta T_h \right] dV + \int_{\Omega_\chi} k \nabla T_h \cdot \nabla (\delta T_h) \, dV \\
\quad + \int_{\Omega_\chi} \tau_\theta \rho_o c \left[\mathbf{c}_h \cdot \nabla (\delta T_h) (\mathbf{c}_h \cdot \nabla T_h - \Pi_h^\theta) \right] dV \\
\quad = W_{ther}^{ext}(\delta T_h) \qquad\qquad\qquad\qquad \forall \delta T_h \\
\int_{\Omega_\chi} \left[(\mathbf{c}_h \cdot \nabla T_h) \delta \Pi_h^\theta \right] dV - \int_{\Omega_\chi} \left(\Pi_h^\theta \cdot \delta \Pi_h^\theta \right) dV = 0 \quad \forall \delta \Pi_h^\theta.
\end{cases}
\tag{63}
$$

6. FSW zones interaction

According to the domain subdivision introduced to deal with the kinematics of the FSW process, there exist two different kind of domain interactions to be discussed. On one side, the link between the mesh of the work-piece (fixed) and the mesh used for the stir-zone, which is rotating according to the pin motion. On the other side, the thermo-mechanical contact behavior between the stir-zone and the pin.

6.1. Modeling the work-piece/stir-zone interaction

When modeling the interface between the work-piece and the stir-zone, the objective is to get continuous fields for all the state variables $\mathbf{v}, p$ and T crossing the interface between the two domains. Work-piece and stir-zone are parts of the same metal sheet even if there exists a relative movement of the two computational sub-domains.

In this work, two different solutions to deal with the interaction at the contact interface between the stir-zone and the work-piece are considered.

The simplest solution consists of assuming both coincident and equi-spaced meshes at the interface. This means that for each boundary node of the stir-zone there exists a corresponding node on the surface of the work-piece. This connection must be kept at each time-step of the simulation that is after any mesh sliding (rotation). This is easy to achieve for 2D analyses but it is much more demanding for an automatic 3D mesh generator, which usually supports unstructured tetrahedral meshes.

When considering coincident surface meshes, it is easy to connect the integration domains by prescribing all the state variables $\mathbf{v}, p$ and T on one side (work-piece surface) to the corresponding values on the other side (stir-zone surface). From the
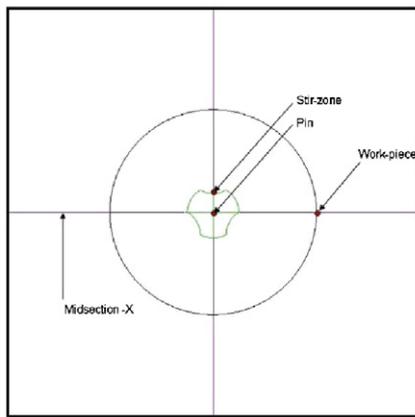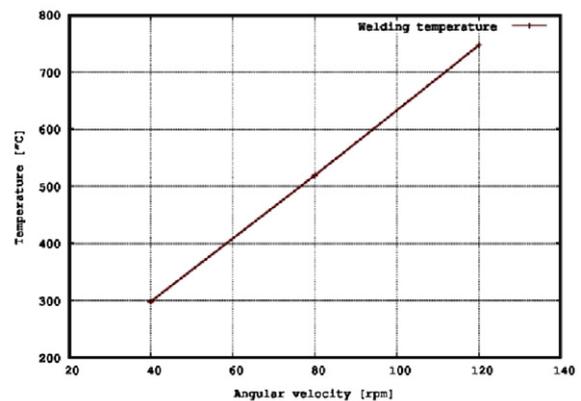
(a) Locations of various virtual-thermocouples and midsection line.
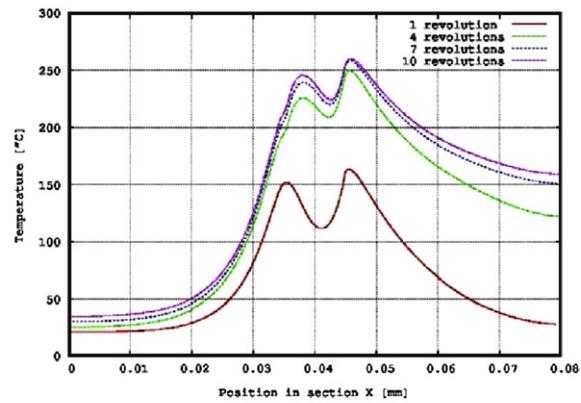
(b) Line-graph along the midsection of the temperature after 1, 4, 7 and 10 revolutions.
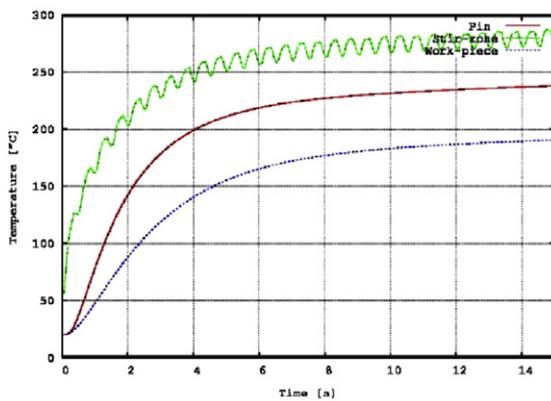
(c) Temperature evolution during the first 10 revolutions at three different locations: center of the pin, in the stir-zone close to the pin and at the border between the stir-zone and the rest of the work-piece.

(d) Maximum welding temperature at the stir-zone close to the pin as a function of the pin-rotation velocity.

Fig. 7. Triflute pin FSW analysis: temperature evolution at different thermocouple locations.

computational point of view, this procedure consists of two steps. Firstly, it is necessary to set a time-step which ensures a perfect node-to-node matching after each mesh sliding. Then, using a search-algorithm (restricted to the interface nodes), it is necessary to identify all the node-to-node (master/slave) connections at the contact interface. Secondly, during the assembling procedure the contributions (elemental residuals and tangent matrices) of the slave nodes are assembled together with the corresponding contributions of the master nodes.

The solution is more complex when there is no perfect match between the master (a coarser mesh is usually defined for the work-piece) and the slave (finer mesh for the stir-zone) surfaces. In this case the strategy adopted consists of projecting each slave node on the master surface to build-up the contact elements all over the contact interface. Once the slave/master contact elements have been generated, one of following three approaches is commonly pursued: the Lagrange multiplier method, the augmented Lagrange method, or the penalty method. The simplest approach is the *penalty method* [1], where very large values (pen-

alty parameters) of both stiffness and thermal resistivity are assigned to the contact elements to ensure the most rigid/conductive behavior between the two domains in both the mechanical and the thermal problems. Also in this case, the contact elements must be re-constructed at each time-step according to a (rather time-consuming) closest-point-projection algorithm.

6.2. Modeling the pin/stir-zone interaction

When modeling the interaction between the pin and the stir-zone the two sub-domains are rotating together. This does not mean that the material moves with the same velocity at the two sides of the contact interface.

Let us denote by, $\mathbf{v}^{pin}$, the velocity at the pin surface and, $\mathbf{v}^{sz}$, the velocity at the stir-zone surface for each contact point of the pin/stir-zone interaction. The relative slip velocity, $\Delta\mathbf{v}_c$, is defined as:

$$\Delta\mathbf{v}_c = \mathbf{v}^{pin} - \mathbf{v}^{sz}. \tag{64}$$

When the pin is plunged into the metal sheet the velocity field at the stir zone is zero, so that the slip velocity is maximum, $\Delta\mathbf{v}_c = \mathbf{v}^{pin}$. During the transition to the steady-state, the material at the stir-zone surface accelerates to fulfill the stationary sticking condition, $\Delta\mathbf{v}_c \to 0$, that is $\mathbf{v}^{sz} \to \mathbf{v}^{pin}$.

This given, two different situations may occur: either sticking or sliding conditions.

We refer to as *sliding condition* when it exists a relative slip between the contacting surfaces:

$$\text{Sliding} \quad \|\mathbf{v}^{pin}\| > \|\mathbf{v}^{sz}\|. \tag{65}$$

The *sticking condition* is achieved when the material at the stir-zone of the contact surface sticks to the pin surface:

$$\text{Sticking} \quad \mathbf{v}^{pin} = \mathbf{v}^{sz}. \tag{66}$$

In FSW the sticking/sliding condition changes continuously and strongly depends on several parameters such as the normal pressure or the temperature field generated by the friction or the plastic dissipation processes.

6.2.1. Coulomb's friction law

Let us define the slip function as:

$$\phi(\mathbf{t}_N, \mathbf{t}_T) = \|\mathbf{t}_T\| - \eta\|\mathbf{t}_N\| \leqslant 0, \tag{67}$$

where η is the friction coefficient and $\mathbf{t}_N$ and $\mathbf{t}_T$ are the normal (pressure) and the tangential (shear) components of the traction vector, $\mathbf{t}_c = \boldsymbol{\sigma} \cdot \mathbf{n}$, at the contact interface, defined as:

$$\mathbf{t}_N = (\mathbf{n} \otimes \mathbf{n}) \cdot \mathbf{t}_c = (\mathbf{t}_c \cdot \mathbf{n})\mathbf{n}, \tag{68}$$
$$\mathbf{t}_T = (\mathbf{I} - \mathbf{n} \otimes \mathbf{n}) \cdot \mathbf{t}_c = \mathbf{t}_c - \mathbf{t}_N, \tag{69}$$

where $\mathbf{n}$ is the unit vector normal to the contact interface.

The slip velocity, $\Delta\mathbf{v}_c$, can be also split into normal and tangential components, $\Delta\mathbf{v}_N$ and $\Delta\mathbf{v}_T$, respectively:

$$\Delta\mathbf{v}_N = (\mathbf{n} \otimes \mathbf{n}) \cdot \Delta\mathbf{v}_c = (\Delta\mathbf{v}_c \cdot \mathbf{n})\mathbf{n}, \tag{70}$$
$$\Delta\mathbf{v}_T = (\mathbf{I} - \mathbf{n} \otimes \mathbf{n}) \cdot \Delta\mathbf{v}_c = \Delta\mathbf{v}_c - \Delta\mathbf{v}_N. \tag{71}$$

This given, in conventional *Coulomb's friction law*, the friction shear stress, $\mathbf{t}_T$, cannot exceed the admissible shear stress, τ_{max}, so that the *sticking condition* is fulfilled when:

$$\text{Sticking} \quad \|\mathbf{t}_T\| < \tau_{max} \to \mathbf{v}^{pin} = \mathbf{v}^{sz}. \tag{72}$$

The *sliding condition* is achieved when the friction shear stress rises up to the admissible shear stress and a relative slip velocity exists between the contacting surfaces:

$$\text{Sliding} \quad \|\mathbf{t}_T\| = \tau_{max} \to \|\mathbf{v}^{pin}\| > \|\mathbf{v}^{sz}\|. \tag{73}$$

Let us define the following (regularized) definition of the tangential component, $\|\mathbf{t}_T\|$, of the traction vector:

$$\|\mathbf{t}_T\| = \varepsilon_T\left(\|\Delta\mathbf{v}_T\| - \dot{\gamma}\frac{\partial\phi}{\partial\|\mathbf{t}_T\|}\right) = \varepsilon_T(\|\Delta\mathbf{v}_T\| - \dot{\gamma}) \tag{74}$$

This is a regularization (penalty method) of the Heaviside (step) function typical of the frictional contact behavior, where ε_T is the corresponding penalty parameter (for more details see [2]).

Using the Kuhn–Tucker conditions:

$$\begin{aligned} \phi &\leqslant 0, \\ \dot{\gamma} &\geqslant 0, \\ \phi\dot{\gamma} &= 0 \end{aligned} \tag{75}$$

defined in terms of the slip function (67) and the slip multiplier, $\dot{\gamma}$, it is possible to recover both the sticking and the sliding mechanisms in a very simple form.

- The *sliding condition* is achieved for $\phi = 0$. In this case, the tangential component of the traction vector, $\mathbf{t}_T$, is given by:

$$\mathbf{t}_T = \tau_{max}\mathbf{u}_T, \tag{76}$$

where τ_{max} is obtained from Eq. (67) as:

$$\tau_{max} = \eta\|\mathbf{t}_N\| \tag{77}$$

while the tangential unit vector, $\mathbf{u}_T$, is computed as:

$$\mathbf{u}_T = \frac{\Delta\mathbf{v}_T}{\|\Delta\mathbf{v}_T\|}. \tag{78}$$

The normal component of the traction vector is obtained with a further penalization as:

$$\mathbf{t}_N = \varepsilon_N\Delta\mathbf{v}_N, \tag{79}$$

where ε_N is the normal penalty parameter, which is enforcing the stick condition in the normal direction.

- The *stick condition* is achieved for $\dot{\gamma} = 0$. The tangential component of the traction vector is obtained from Eqs. (74) and (78) as:

$$\mathbf{t}_T = \varepsilon_T\Delta\mathbf{v}_T$$

and the normal component of the traction vector is given by Eq. (79).

Remark-1: Eqs. (74) and (75) have the same format as in classical J2 plasticity (see [2]): in that case, ϕ, is representing the yield surface and, $\dot{\gamma}$, the plastic multiplier.

Remark-2: The penalty method, introduced to regularize the contact problem, is an elegant format to circumvent the numerical difficulties of the discontinuous solution. However, the choice of the penalty parameters remains a difficult task. On one side, high values approximate better the Heaviside (step) function, but at the same time they lead to ill-conditioning of the solution matrix. On the other side, the use of lower values for the penalization retains the stick condition for too long.

Remark-3: The friction coefficient, $\eta(T, \Delta\mathbf{v}_c)$, is a highly non-linear function of both the surface temperature, T, and the relative slip velocity, $\Delta\mathbf{v}_c$, making the calibration of the Coulomb's law in the transient phase of the FSW process difficult [8].

6.2.2. Norton's friction law

In most of the FSW processes the sliding condition is predominant, so that even if the material close to the pin surface is accelerated, in practice, it never reaches the tool velocity (sticking condition). In the sliding condition, the Coulomb's law is a poor representation of the frictional phenomena which depends on a constant friction coefficient. The *Norton's friction law* shows a more realistic behavior, taking into account both the surface temperature and the relative sliding velocity [8]. This friction law can be written in compact form as:

$$\mathbf{t}_T = \eta_{eq}\mathbf{u}_T \tag{80}$$

and the equivalent friction coefficient, $\eta_{eq}(T, \Delta\mathbf{v}_T)$, is expressed as:

$$\eta_{eq} = a(T)\|\Delta\mathbf{v}_T\|^q, \tag{81}$$

where $a(T)$ is the (temperature dependent) material consistency and $0 \leqslant q \leqslant 1$ is the strain rate sensitivity. For $q = 0$, the Coulomb's law is recovered and $a(T)$ represents the (temperature dependent) admissible shear stress, τ_{max}.

Two alternative implementation strategies are possible depending on the mesh generated at the contact interface.

On one hand, if the surface meshes of pin (master) and stir-zone (slave) are non-coincident, the first step consists of generating the contact elements: all slave nodes are projected onto the best matching master facet (discretized counterpart of the master sur-

face) according to a classical closest-point projection algorithm. Each contact element is built up using the slave node and the nodes belonging to the selected master facet. Both the elemental residual and stiffness matrix are split into normal and tangential contributions. Hence, the thermo-mechanical contact interaction is guaranteed by enforcing the continuity of both normal and tangential components of the traction vector:

$$\mathbf{t}_N^{pin} = -\mathbf{t}_N^{sz}, \tag{82}$$

$$\mathbf{t}_T^{pin} = -\mathbf{t}_T^{sz}. \tag{83}$$

In a similar way, the heat flux crossing the surface must satisfy:

$$q^{pin} = -q^{sz}, \tag{84}$$

where the heat flux, q, is computed using *Newton's law* (see [23]), defined in terms of the temperature gap and the heat transfer coefficient, h_c:

$$q^{pin} = h_c\left(T^{pin} - T^{sz}\right), \tag{85}$$

$$q^{sz} = h_c\left(T^{sz} - T^{pin}\right). \tag{86}$$

On the other hand, it is very interesting to consider the case of coincident surface discretization at the contact interface. In this case, there is a *node-to-node* correspondence and it is not necessary to generate contact elements. Furthermore, the rotation of slave and master surfaces is synchronized so that a searching operation at each time-step is not necessary. The main advantage of using coincident meshes consists of avoiding the use of penalty parameters for the stick condition. Slave and master nodes can be linked together using the same (master) nodal variables:

$$\mathbf{v}^{pin} = \mathbf{v}^{sz}. \tag{87}$$

For the slip condition, it is necessary to split the velocity field at the interface into normal and tangential components: the normal component is treated as for the stick condition while in the tangential direction is necessary to enforce the continuity of the tangential traction vector as:

$$\mathbf{v}_N^{pin} = \mathbf{v}_N^{sz}, \tag{88}$$

$$\mathbf{t}_T^{pin} = -\mathbf{t}_T^{sz}. \tag{89}$$

Finally, in the numerical simulation of the FSW process, it is important to account for the heat flux induced by the friction dissipation, as this is the key mechanisms of heat generation during the welding process. When the sliding condition is satisfied, the heat flux generated by the friction dissipation in both Norton and Coulomb (as a particular case when the rate sensitivity parameter $q = 0$) friction laws is computed as:

$$q_{frict}^{pin} = \vartheta^{pin}[\mathbf{t}_T \cdot \Delta\mathbf{v}_T] = \vartheta^{pin}a(T)\|\Delta\mathbf{v}_T\|^{q+1}, \tag{90}$$

$$q_{frict}^{sz} = \vartheta^{sz}[\mathbf{t}_T \cdot \Delta\mathbf{v}_T] = \vartheta^{sz}\ a(T)\|\Delta\mathbf{v}_T\|^{q+1} \tag{91}$$

so that the total amount of heat generated during the friction dissipation is split into the fraction absorbed by the pin ϑ^{pin} and the fraction absorbed by the work-piece in the stir-zone $\vartheta^{sz} = 1 - \vartheta^{pin}$, computed respectively as:

$$\vartheta^{pin} = \frac{\alpha^{pin}}{\alpha^{pin} + \alpha^{sz}}, \tag{92}$$

$$\vartheta^{sz} = \frac{\alpha^{sz}}{\alpha^{pin} + \alpha^{sz}}, \tag{93}$$

where $\alpha = \frac{k}{\rho_o c}$ is the thermal diffusivity of the material. The more diffusive is the material (compared to the other one) the more heat it absorbs (e.g. welding aluminum with a steel pin: $\vartheta^{pin} \approx 0.8$ and $\vartheta^{sz} \approx 0.2$).

7. Numerical simulations

The formulation presented in the previous sections is illustrated here with a number of numerical simulations. The goals are two-fold: firstly, to demonstrate the accuracy of the proposed ALE kinematic formulation comparing the results with a reference solution; secondly, to show the FSW simulation capabilities accounting for both stirring and frictional effects when using a non-cylindrical pin.

Computations are performed using the in-house finite element code COMET [16] developed by the authors at the International Center for Numerical Method in Engineering (CIMNE) in Barcelona, Spain. The post-processing of the results has been carried out using the pre and postprocessor GiD also developed at CIMNE [41].

7.1. ALE formulation benchmark

Fig. 2(a) represents a square domain of 80×80 [mm²]. This computational domain is divided in two different areas (gray and blue) where the circular section has a diameter of 40 [mm].

An inflow velocity of 0.01 [m/s] is imposed at the left side of the domain, representing the body movement from right to left. Vertical velocity is prescribed to zero at the top and bottom side of the domain. The initial temperature field consists of a linear distribution varying from the top side (50 °C) to the bottom side (−50 °C), defining a constant temperature gradient along the vertical direction. For the sake of simplicity, constant thermo-physical properties have been used to characterize the material (aluminum alloy): $\rho_o = 2600\,[\text{kg/m}^3]$, $c = 900[\text{J}/(\text{kg K})]$ and $k = 150\,[\text{W}/(\text{m K})]$, corresponding to the density, the specific heat and the thermal conductivity, respectively.

The FE discretization of the computational domain is presented in Fig. 2(b). It consists of 12,453 nodes and 24,744 triangular elements with an average size of 0.5 [mm] in the blue area and 1.0 [mm] in the gray zone.

Using an Eulerian approach, the solution of this problem is simple: it is a rigid movement defined by a constant velocity field (the inflow velocity) and a null pressure field. The Eulerian formulation also solves the thermal problem exactly because the convective term is null by *construction*: the velocity is orthogonal to the temperature gradient everywhere. Hence, the initial temperature field is also the steady-state solution of the problem as shown in Fig. 3(a).

The purpose of this numerical example is to show the accuracy of the proposed ALE formulation solving the same problem when the mesh in the blue area is rotating (anti-clockwise) with an angular velocity of 40, 80 and 120 [rpm], respectively. This problem presents the same kind of difficulties of a FSW simulation where the gray zone represents the work-piece, while the blue area stands for the stir-zone which is rotating together with the pin. The selected values for the angular velocity are in the range commonly used for industrial aluminum FSW process.

In this case, the thermal solution is not exact because the convective term due to the mesh movement must be solved: $\mathbf{c} \cdot \nabla T = -\mathbf{v}_{mesh} \cdot \nabla T \neq 0$. The Courant number, defined as $Cu = \|\mathbf{v}_{mesh}\|\frac{\Delta t}{h_e}$, is useful to check the accuracy of the solution in terms of selected mesh size h_e, and the time-increment, Δt chosen.

Forcing node-to-node mesh synchronization at the interface between the gray and the blue domains, then $Cu \leqslant 1$ in all the blue domain and null in the gray area. At the sliding interface $Cu = 1$. This is the maximum value in all the computational area, preserving the accuracy of the solution. A fixed number of 251 time-steps are necessary to complete one revolution, which corresponds to the number of elements at the sliding interface. Table 3 shows the time-increment, Δt, used in the simulations.

Fig. 3 show the temperature contour-fill after one full rotation of the blue domain. It is possible to notice a very small perturbation of the temperature gradient proportional to the angular velocity. However, the error introduced in the ALE domain by the convective term does not compromise the accuracy of the analysis. Higher rotation velocities could require finer mesh discretization and the corresponding reduced time-stepping to keep the Courant number, $Cu \leqslant 1$.

7.2. Triflute pin FSW analysis

The next example demonstrates the performance of the proposed formulation when simulating a real-case FSW process. Using the same square domain presented in the previous example a triflute pin (green area) is added in the middle of the stir-zone (blue domain), as shown in Fig. 4(b).

The pin shape is obtained starting from an original circular section (green area) with a diameter of 10 [mm] where three circular segments have been removed as detailed in Fig. 4(a). The white circles have the same diameter (10 [mm]) than the green one and the distance between the center of each white circle and the center of the green one is 8.66 [mm] leading to a subdivision of the circumference of the green circle in six equal parts.

The corresponding mesh is shown in Fig. 4 and a detail of the FE discretization close to the pin is presented in Fig. 4(d). This mesh is exactly the same (12,453 nodes and 24,744 triangular elements) used in the ALE benchmark but, in this case, the green area represents the triflute pin. This FE discretization has proved to guarantee sufficient accuracy when solving the thermo-mechanical problem (a finer mesh does not significantly modify neither the temperature nor the velocity field).

The simulations have been carried out considering a Norton–Hoff model with constant effective viscosity, $\mu_{eff} = 100$ [MPa/s] and a constant exponent, $m = 0.2$, for both the work-piece and the stir-zone. The pin is assumed to be rigid. The thermo-physical properties (density, specific heat and thermal conductivity) used to characterize the aluminum sheet are the same as in the previous benchmark while the pin has been characterized by typical thermo-physical properties of a steel: $\rho_o = 7800$ [kg/m^3], $c = 500$ [J/(kg K)] and $k = 25$ [W/(m K)], respectively.

The welding parameters are given in terms of constant advancing velocity 0.010 [m/s] and different constant rotational (anti-clockwise) angular velocity: 40, 80 and 120 [rpm], respectively. In the simulations the pin is rotating around a fixed axis while the metal-sheet moves towards the pin from the left to right (which corresponds to the pin advancing movement from right to left). The initial (uniform) temperature for all the welding tools is 20 °C.

Perfect stick (infinite frictional coefficient) is prescribed at the interface between the pin (green) and the stir-zone (blue). This hypothesis is realistic when welding aluminum with steel tools. The interface between the stir-zone (blue) and the rest of the work-piece (gray) is treated as for the ALE benchmark: a sliding motion enforces node-to-node mesh synchronization to keep the Courant number, $Cu \leqslant 1$ in all the domain, preserving the accuracy of the solution. The time increments used are those in Table 3.

Fig. 5(a) and (b) show the velocity and pressure contour-fill, respectively, for the angular velocity of 40 [rpm]. It is interesting to note the quality of the pressure field, free of any spurious oscillation thanks to the OSS stabilization technique adopted to deal with the incompressibility condition.

Fig. 5(c) shows the velocity vectors in the stir-zone close to the pin. Here, the triflute shape seems not to be so relevant for the material stirring and the pin effectively acts as a circular FSW tool. The material entrapped in the circular segments is transported following the pin motion as clearly manifested by the stream-lines in Fig. 5(d).

Fig. 6 shows the temperature field after 1, 4, 7 and 10 revolutions, respectively. The initially uniform temperature field is affected by the heat generated either by the plastic dissipation due to the material stirring or by the frictional mechanism at the pin/stir-zone interface.

Fig. 7(a) defines the position of the midsection line and the location of three virtual-thermocouples (at the center of the pin, in the stir-zone close to the pin and at the border between the stir-zone and the rest of the work-piece) where the temperature evolution is recorded. Fig. 7(b) shows the temperature variation along the midsection after 1, 4, 7 and 10 revolutions, respectively. On one hand, the lower thermal diffusivity of the pin (steel-made) causes the two picks in all the curves. On the other hand, after 10 revolutions the temperature field is very close to the steady-state value and the numerical simulation can be terminated. Fig. 7(c) shows the temperature evolution at the location of the three virtual-thermocouples: in all cases the temperature is close to the steady-state condition and reaches the maximum value at the pin/stir-zone interface. Finally, Fig. 7(d) shows the maximum temperature attained at the pin/stir-zone interface for different pin-rotation velocities: 40 [rpm], 80 [rpm] and 120 [rpm], respectively. The relationship between angular velocity and maximum temperature achieved is mostly linear and the optimal pin-rotation velocity which guarantees a working temperature close to the melting point is in the range of 90 [rpm].

8. Conclusions

This work presents the strategy adopted for the numerical simulation of the FSW process. A coupled thermo-mechanical solution of both the momentum and energy balance equations is presented. A very general kinematic framework has been used to deal with the specific description of motion in the FSW problem. More in detail, the ALE formulation of the balance equations has been introduced to describe the relationship between the material and the mesh movement in the stir-zone. This formulation includes, as limit cases, either the Eulerian framework for the rest of the metal sheet while moving toward the pin or the Lagrangian description used to follow the pin rotation. The two different mechanisms of heat generation coming from stirring and friction have been described, coupling the mechanical and thermal models. In the hypothesis of incompressible material behavior the stabilized mixed $\mathbf{v}/p$ formulation has been used due to the good performance of this technology, especially for industrial simulations when triangular/tetrahedral meshes must be used for the domain discretization. Following the same strategy, the convective term in the thermal partition has been stabilized using the same OSS stabilization, leading to a very accurate treatment of this phenomenon. The numerical benchmarks have shown the accuracy of both the thermal and the mechanical responses when a FSW process is simulated.

Acknowledgments

References

[1] C. Agelet de Saracibar, A new frictional time integration algorithm for large slip multi-body frictional contact problems, Comput. Methods Appl. Mech. Engrg. 142 (3–4) (1997) 303–334.

[2] C. Agelet de Saracibar, M. Chiumenti, On the numerical modeling of frictional wear phenomena, Comput. Methods Appl. Mech. Engrg. 177 (1998) 401–426.

[3] C. Agelet de Saracibar, M. Cervera, M. Chiumenti, On the formulation of coupled thermoplastic problems with phase-change, Int. J. Plasticity 15 (1999) 1–34.

[4] C. Agelet de Saracibar, M. Cervera, M. Chiumenti, On the constitutive modelling of coupled thermo-mechanical phase-change problems, Int. J. Plasticity 17 (2001) 1565–1622.

[5] C. Agelet de Saracibar, M. Chiumenti, Q. Valverde, M. Cervera, On the orthogonal subgrid scale pressure stabilization of finite deformation J2 plasticity, Comput. Methods Appl. Mech. Engrg. 195 (2006) 1224–1251.

[6] F. Armero, J.C. Simo, A new unconditionally stable fractional step method for nonlinear coupled thermomechanical problems, Int. J. Numer. Methods Engrg. 35 (1991) 737–766.

[7] F. Armero, J.C. Simo, Product Formula Algorithms for Nonlinear Coupled Thermoplasticity: Formulation and Nonlinear Stability Analysis, Sudam Report #92-4, Department of Mechanical Engineering, Stanford University, Stanford, California, 1992.

[8] M. Assidi, L. Fourment, Accurate 3D friction stir welding simulation tool based on friction model calibration, Int. J. Mater. Forming 2 (1) (2009) 327–330, http://dx.doi.org/10.1007/s12289-009-0541-6.

[9] M. Assidi, L. Fourment, S. Guerdoux, T. Nelson, Friction model for friction stir welding process simulation: calibrations from welding experiments, Int. J. Machine Tools Manuf. 50 (2010) 143–155.

[10] T. Belytschko, J.M. Kennedy, Computer methods for subassembly simulation, Nucl. Engrg. Des. 49 (1978) 17–38.

[11] T. Belytschko, J.M. Kennedy, D.F. Schoeberle, Quasi-Eulerian finite element formulation for fluid–structure interaction, J. Press. Vess. Technol. 102 (1980) 62–69.

[12] T. Belytschko, D.P. Flanagan, J.M. Kennedy, Finite element methods with user-controlled meshes for fluid–structure interaction, Comput. Methods Appl. Mech. Engrg. 33 (1982) 669–688.

[13] R. Boman, J.P. Ponthot, Efficient ALE mesh management for 3D quasi-Eulerian problems, Int. J. Numer. Methods Engrg. (2012), http://dx.doi.org/10.1002/nme.4361.

[14] F. Brezzi, M. Fortin, Mixed and Hybrid Finite Element Methods, Springer, New York, 1991.

[15] M. Cervera, C. Agelet de Saracibar, M. Chiumenti, Thermo-mechanical analysis of industrial solidification processes, Int. J. Numer. Methods Engrg. 46 (1999) 1575–1591.

[16] M. Cervera, C. Agelet de Saracibar, M. Chiumenti, COMET: Coupled Mechanical and Thermal Analysis, Data Input Manual, Version 5. 0, Technical Report IT-308, 2002. <http://www.cimne.upc.es>.

[17] M. Cervera, M. Chiumenti, Q. Valverde, C. Agelet de Saracibar, Mixed linear/linear simplicial elements for incompressible elasticity and plasticity, Comput. Methods Appl. Mech. Engrg. 192 (2003) 5249–5263.

[18] Y.J. Chao, X. Qi, Thermal and thermo-mechanical modeling of friction stir welding of aluminum alloy 6061-T6, J. Mater. Process. Manuf. Sci. 7 (1998) 215–233.

[19] Y.J. Chao, X. Qi, Heat transfer and thermo-mechanical modeling of friction stir joining of AA6061-T6 plates, in: Proceedings of the First International Symposium on Friction Stir Welding, Thousand Oaks, CA, USA, 1999.

[20] Y.J. Chao, X. Qi, W. Tang, Heat transfer in friction stir welding: experimental and numerical studies, ASME J. Manuf. Sci. Engrg. 125 (2003) 138–145.

[21] M. Chiumenti, Q. Valverde, C. Agelet de Saracibar, M. Cervera, A stabilized formulation for elasticity using linear displacement and pressure interpolations, Comput. Methods Appl. Mech. Engrg. 191 (2002) 5253–5264.

[22] M. Chiumenti, Q. Valverde, C. Agelet de Saracibar, M. Cervera, A stabilized formulation for incompressible plasticity using linear triangles and tetrahedra, Int. J. Plasticity 20 (2004) 1487–1504.

[23] M. Chiumenti, C. Agelet de Saracibar, M. Cervera, On the numerical modeling of the thermo-mechanical contact for casting analysis, J. Heat Transfer 130 (6) (2008). 061301 (10 pages).

[24] A. Chorin, T.J.R. Hughes, M.F. McCracken, J.E. Marsden, Product formulas and numerical algorithms, Commun. Pure Appl. Math. 31 (1978) 205–256.

[25] P. Colegrove, M. Pinter, D. Graham, T. Miller, Three dimensional flow and thermal modeling of the friction stir welding process, in: Second International Symposium on Friction Stir Welding, June 26–28, Gothenburg, Sweden, 2000.

[26] R. Codina, Stabilization of incompressibility and convection through orthogonal sub-scales in finite element methods, Comput. Methods Appl. Mech. Engrg. 190 (2000) 1579–1599.

[27] R. Codina, Stabilized finite element approximation of transient incompressible flows using orthogonal subscales, Comput. Methods Appl. Mech. Engrg. 191 (2002) 4295–4321.

[28] R. Codina, J. Blasco, Stabilized finite element method for transient Navier–Stokes equations based on pressure gradient projection, Comput. Methods Appl. Mech. Engrg. 182 (2000) 287–300.

[29] C.J. Dawes, An introduction to friction stir welding butt welding and its developments, Welding Met. Fabrication 63 (1995) 13–16.

[30] T. De Vuyst, L. D'Alvise, A. Robineau, J.C. Goussain, Material flow around a friction stir welding tool: experiment and Simulation, in: 8th International Seminar on Numerical Analysis of Weldability, Graz, Austria, 2006.

[31] T. De Vuyst, L. D'Alvise, A. Robineau, J.C. Goussain, Simulation of the material flow around a friction stir welding tool, in: TWI 6th International Symposium on FSW, October 10–12, Saint-Sauveur, Canada, 2006.

[32] T. Dickerson, H. Shercliff, H. Schmidt, A weld marker technique for flow visualization in friction stir welding, in: 4th International Symposium on Friction Stir Welding, Park City, Utah, USA, 2003.

[33] J. Donea, Finite element analysis of transient dynamic fluid–structure interaction, in: J. Donéa (Ed.), Advanced Structural Dynamics, Springer, 1978, pp. 255–290.

[34] J. Donea, S. Giuliani, J.P. Halleux, An arbitrary Lagrangian–Eulerian finite element method for transient dynamic fluid–structure interactions, Comput. Methods Appl. Mech. Engrg. 33 (1–3) (1982) 689–723.

[35] J. Donea, Arbitrary Lagrangian–Eulerian finite element methods, in: T.J.R. Hughes, T. Belytschko (Eds.), Computational Methods for Transient Analysis, North-Holland, Amsterdam, 1983, pp. 474–516.

[36] J. Donea, A. Huerta, J.-P. Ponthot, A. Rodrí guez-Ferran, Arbitrary Lagrangian–Eulerian methods. Encyclopedia of computational mechanics, in: E. Stein, R. de Borst, T.J.R. Hughes (Eds.), Fundamentals, vol. 1, John Wiley & Sons, Ltd., 2004. ISBN: 0-470-84699-2.

[37] P. Dong, F. Lu, J.K. Hong, Z. Cao, Coupled thermomechanical analysis of friction stir welding process using simplified models, Sci. Technol. Weld. Jointing 6 (2001) 281–287.

[38] C.D. Donne, E. Lima, J. Wegener, A. Pyzalla, T. Buslaps, Investigations on residual stresses in friction stir welds, in: Third International Symposium on Friction Stir Welding, Sept. 27–28, Kobe, Japan, 2001.

[39] R.M. Frank, R.B. Lazarus, Mixed Eulerian–Lagrangian method, in: B. Alder et al. (Eds.), Methods in Computational Physics, Academic Press, New York, 1964, p. 3.

[40] O. Frigaard, O. Grong, O.T. Midling, A process model for friction stir welding of age hardening aluminum alloys, Metal. Mater. Transition A 32 (2001) 1189–1200.

[41] GiD: The personal pre and post preprocessor, 2002. <http://www.gidhome.com>.

[42] J. Gould, Z. Feng, Heat flow model for friction stir welding of aluminum alloys, J. Mater. Process. Manuf. Sci. 7 (1998) 185–194.

[43] M. Guerra, C. Schmids, J.C. McClure, L.E. Murr, A.C. Nunes, Flow patterns during friction stir welding, Mater. Characterization 49 (2003) 95–101.

[44] A. Hansel, T. Spittel, Kraft- und Arbeitsbedarf Bildsamer Formgebungsverfahren, VEB Deutscher Verlag fur Grundstoffindustrie, Leipzig, 1979.

[45] A. Huerta, F. Casadei, New ALE applications in nonlinear fast-transient solid dynamics, Engrg. Comput. 11 (4) (1994) 317–345.

[46] H.J. Hoff, Approximate analysis of structures in presence of moderately large creep deformation, Quart. Appl. Math. 12 (1954) 49.

[47] T.J.R. Hughes, W.K. Liu, T.K. Zimmermann, Lagrangian–Eulerian finite element formulation for incompressible viscous flows, Comput. Methods Appl. Mech. Engrg. 29 (3) (1981) 329–349.

[48] T.J.R. Hughes, Multiscale phenomena: Green's function, Dirichlet to Neumann formulation, subgrid scale models, bubbles and the origins of stabilized formulations, Comput. Methods Appl. Mech. Engrg. 127 (1995) 387–401.

[49] A.M. Jorge Jr., O. Balancín, Prediction of steel flow stresses under hot working conditions, Mater. Res. 8 (3) (2004) 309–315.

[50] O.T. Midling, Effect of tool shoulder material on heat input during friction stir welding, in: First International Symposium on Friction Stir Welding, June14–16, Thousands Oaks, CA, USA, 1999.

[51] R.M. Mishra, M.W. Mahoney, Friction Stir Welding & Processing, ASM International, 2007.

[52] W.F. Noh, CEL: a time-dependent two-space dimensional coupled Eulerian–Lagrangian code, in: B. Alder, S. Fernbach, M. Rotenberg (Eds.), Methods in Computational Physics, vol. 3, Academic Press, New York, 1964, pp. 117–179.

[53] F.H. Norton, The Creep of Steel at Hight Temperature, McGraw Hill, New York, USA, 1924.

[54] E. Oñate, J. Rojek, R.L. Taylor, O.C. Zienkiewicz, Finite calculus formulation for incompressible solids using linear triangles and tetrahedra, Int. J. Numer. Methods Engrg. 59 (2004) 1473–1500, http://dx.doi.org/10.1002/nme.922.

[55] J.P. Ponthot, M. Hogge, The use of the Eulerian–Lagrangian FEM in metal forming applications including contact and adaptive mesh, in: N. Chandra, J.N. Reddy (Eds.), Advances in Finite Deformation Problems in Material Processing, ASME Winter Annual Meeting, ASME, American Society of Mechanical Engineers, AMD-125, Atlanta, 1991, pp. 44–64.

[56] J.P. Ponthot, T. Belytschko, Arbitrary Lagrangian–Eulerian formulation for element-free Galerkin method, Comput. Methods Appl. Mech. Engrg. 152 (1–2) (1998) 19–46.

[57] G. Quan, K. Liu, J. Zhou, B. Chen, Dynamic softening behaviors of 7075 aluminum alloy, Trans. Nonferrous Metals Soc. China 19 (2009) 537–541, http://dx.doi.org/10.1016/S1003-6326(10)60104-5.

[58] A. Rodriguez-Ferran, F. Casadei, A. Huerta, ALE stress update for transient and quasistatic processes, Int. J. Numer. Methods Engrg. 43 (1998) 241–262.

[59] M.J. Russell, H.R. Sheercliff, Analytic modeling of microstructure development in friction stir welding, in: First International Symposium on Friction Stir Welding, June 14–16, Thousands Oaks, CA, USA, 1999.

[60] D. Santiago, G. Lombera, S. Urquiza, A. Cassanelli, L.A. de Vedia, Numerical modelling of welded joints by the friction stir welding process, Mater. Res. 7 (4) (2004) 569–574.

[61] D. Santiago, G. Lombera, S. Urquiza, C. Agelet de Saracibar, M. Chiumenti, Modelado termomecánico del proceso de Friction Stir Welding utilizando la

M. Chiumenti et al./Comput. Methods Appl. Mech. Engrg. 254 (2013) 353–369

369

geometría real de la herramienta, Rev. I. Métodos Num. para Cálculo y Diseño en Ing. 26 (2010) 293–303.

[62] T. Sheppard, D. Wright, Determination of flow stress: Part-1 Constitutive equation for aluminum alloys at elevated temperatures, Met. Technol. 6 (1979) 215–223.

[63] R. Talwar, B. Bolser, R. Lederich, J. Baumann, Friction stir welding of airframe structures, in: Second International Symposium on Friction Stir Welding, June 26–28, Gothenburg, Sweden, 2000.

[64] W. Tang, X. Guo, J.C. McClure, L.E. Murr, A. Nunes, Heat input and temperature distribution in friction stir welding, J. Mater. Process. Manuf. Sci. 7 (1998) 163–172.

[65] M.W. Thomas, J. Nicholas, J.C. Needham, M.G. Murch, P. Templesmith, C.J. Dawes, Friction Stir Butt Welding, GB Patent Application No. 9125978, 8 December 1991, US Patent No. 5460317, October 1995.

[66] W. Thomas, P. Threadgill, E. Nicholas, The feasibility of friction stir welding steel, Sci. Technol. Welding Joining 4 (6) (1999) 365–372.

[67] P. Ulysse, Three-dimensional modelling of the friction stir welding process, Int. J. Machine Tools Manuf. 42 (2002) 1549–1557.

[68] X.K. Zhu, Y.J. Chao, Numerical simulation of transient temperature and residual stresses in friction stir welding of 304L stainless steel, J. Mater. Process. Technol. 146 (2004) 263–272.